PLANT HIGH-THROUGHPUT PHENOTYPING USING PHOTOGRAMMETRY AND 3D MODELING TECHNIQUES

by

NAN AN

M.A., University of Kansas, 2009
B.S., China University of Geosciences, Beijing, 2005

AN ABSTRACT OF A DISSERTATION

submitted in partial fulfillment of the requirements for the degree

DOCTOR OF PHILOSOPHY

Department of Agronomy
College of Agriculture

KANSAS STATE UNIVERSITY
Manhattan, Kansas

2015

Abstract

Plant phenotyping has been studied for decades for understanding the relationship between plant genotype, phenotype, and the surrounding environment. Improved accuracy and efficiency in plant phenotyping is a critical factor in expediting plant breeding and the selection process. In the past, plant phenotypic traits were extracted using invasive and destructive sampling methods and manual measurements, which were time-consuming, labor-intensive, and cost-inefficient. More importantly, the accuracy and consistency of manual methods can be highly variable. In recent years, however, photogrammetry and 3D modeling techniques have been introduced to extract plant phenotypic traits, but no cost-efficient methods using these two techniques have yet been developed for large-scale plant phenotyping studies. High-throughput 3D modeling techniques in plant biology and agriculture are still in the developmental stages, but it is believed that the temporal and spatial resolutions of these systems are well matched to many plant phenotyping needs. Such technology can be used to help rapid phenotypic trait extraction aid crop genotype selection, leading to improvements in crop yield.

In this study, we introduce an automated high-throughput phenotyping pipeline using affordable imaging systems, image processing, and 3D reconstruction algorithms to build 2D mosaicked orthophotos and 3D plant models. Chamber-based and ground-level field implementations can be used to measure phenotypic traits such as leaf length, rosette area in 2D and 3D, plant nastic movement, and diurnal cycles. Our automated pipeline has cross-platform capabilities and a degree of instrument independence, making it suitable for various situations.

PLANT HIGH-THROUGHPUT PHENOTYPING USING PHOTOGRAMMETRY AND 3D MODELING TECHNIQUES

by

NAN AN

M.A., University of Kansas, 2009
B.S., China University of Geosciences, Beijing, 2005

A DISSERTATION

submitted in partial fulfillment of the requirements for the degree

DOCTOR OF PHILOSOPHY

Department of Agronomy
College of Agriculture

KANSAS STATE UNIVERSITY
Manhattan, Kansas

2015

Approved by:

Co-Major Professor
Stephen Welch

Approved by:

Co-Major Professor
Kevin Price

Copyright

Abstract

Plant phenotyping has been studied for decades for understanding the relationship between plant genotype, phenotype, and the surrounding environment. Improved accuracy and efficiency in plant phenotyping is a critical factor in expediting plant breeding and the selection process. In the past, plant phenotypic traits were extracted using invasive and destructive sampling methods and manual measurements, which were time-consuming, labor-intensive, and cost-inefficient. More importantly, the accuracy and consistency of manual methods can be highly variable. In recent years, however, photogrammetry and 3D modeling techniques have been introduced to extract plant phenotypic traits, but no cost-efficient methods using these two techniques have yet been developed for large-scale plant phenotyping studies. High-throughput 3D modeling techniques in plant biology and agriculture are still in the developmental stages, but it is believed that the temporal and spatial resolutions of these systems are well matched to many plant phenotyping needs. Such technology can be used to help rapid phenotypic trait extraction aid crop genotype selection, leading to improvements in crop yield.

In this study, we introduce an automated high-throughput phenotyping pipeline using affordable imaging systems, image processing, and 3D reconstruction algorithms to build 2D mosaicked orthophotos and 3D plant models. Chamber-based and ground-level field implementations can be used to measure phenotypic traits such as leaf length, rosette area in 2D and 3D, plant nastic movement, and diurnal cycles. Our automated pipeline has cross-platform capabilities and a degree of instrument independence, making it suitable for various situations.

Table of Contents

List of Figures

List of Tables

Acknowledgements

I owe a great amount of appreciation to a large number of people who helped me complete my dissertation and guided my career path instrumentally and emotionally.

I would like to express my deepest gratitude to my advisors, mentors, and friends, Dr. Stephen Welch and Dr. Kevin Price. Thank both of you so much for your unconditional support that made it possible for me to complete my dissertation. I will always remember the personal and professional interactions we had over the years. I am grateful for the influence of your personalities and your attitudes on my career, family, and life in general. Both of you not only taught me critical thinking skills as a researcher but also taught me how to reflect and learn from each life experience. I will remember the teachings from both of you for the rest of my life.

I would also like to thank my committee members: Dr. Jesse Poland, Dr. Stephen Egbert, and Dr. Stacy Hutchinson. Your invaluable feedback and suggestions encouraged me to broaden my horizons so I could incorporate them into my dissertation. I would also love to thank Dr. Cynthia Weinig at the University of Wyoming and Dr. Julin Maloof at the University of California, Davis for their support on my project.

I appreciate all of the help and suggestions from my collaborators: Christine Palmer, Robert Baker, Cody Markelz, James Ta, Smita Sharan, Rishab Vaswani, Lakshmi Narjala, Wen Fung Leong, and Huan Wang. All of you provided invaluable help throughout years on this project.

Last but not least, I especially want to thank my parents for believing in me and giving me the autonomy to pursue my dreams. Without your numerous sacrifices and support, I would not have been able to complete my Ph.D. and enjoy my personal and professional growth. To my supportive wife, life partner, and soul mate, Ran Zhao, thank you for standing by me through all

these seven years. I am glad that we have each other to witness many of our life milestones and have shared our laughter and tears together in the past nine years. I am also grateful for the joy, excitement, hope, and love as a father that Dillon and Ian (on the way) have brought to me. Seeing your smile is the most beautiful thing of all.

Dedication

For my parents

My beautiful wife, Ran Zhao

And my lovely boys, Dillon and Ian

Chapter 1 - Introduction

Plant high-throughput phenotyping

Phenotyping is acquiring a set of observable characteristics of plants resulting from the interaction of their genotypes with the environment (Wanscher 1975; Blum et al. 1982). Traditional phenotyping methods often rely on simple tools like rulers and other measuring devices, along with large amounts of manual work, to extract the desired trait data. Compared to advanced genotyping methods such as the latest sequencing technologies, traditional phenotyping methods are time-consuming, labor-intensive, and cost-inefficient. This limits our ability to quantitatively understand how genetic traits are related to plant growth, environmental adaptation, and yield.

In the past several years, tremendous interest in plant high-throughput phenotyping (HTP) techniques has arisen. These techniques use sensor systems and automated computer algorithms to extract phenotypic traits for large genetic mapping populations using non-destructive and non-invasive sampling methods (Fiorani and Schurr 2013). With such new techniques, plant phenotypes can be linked with functional genomics and environmental factors, thus facilitating plant breeding and leading toward improved crop production and yield stability. This is essential to meet the expected demands of the world population by 2050 (Bolon et al. 2011; Bongaarts 2014).

Typically, the extraction of data via HTP methods involves a series of discrete steps that must be reliably executed in sequence. Such a set of steps is referred to as a “pipeline”. Commercial phenotyping systems such as GROWSCREEN*FLUORO (Walter et al. 2007; Jansen et al. 2009), PHENOPSIS (Granier et al. 2006), and the LemnaTec Scanalyzer HTS

(Furbank and Tester 2011; Green et al. 2012; Chen et al. 2014; Dornbusch et al. 2014) have been used in some small-scale research laboratories for automating plant phenotyping in controlled environments. Larger-scale, fully-automated high-throughput phenotyping facilities have also been deployed in the greenhouses or growth chambers of private sector firms such as Monsanto and Dupont Pioneer and in the most advanced national plant research institutions such as the Australian Plant Phenomics Facility, the European Plant Phenotyping Network, and USDA; however, these indoor facilities cannot be used for field phenotyping. Additionally, the cost of these systems is beyond most research laboratories' budgets, thus slowing the advance of science.

In the field, most phenotyping systems have mainly focused on automated solutions for data acquisition using platforms that combine a vehicle and perhaps some robotics with imaging systems and sensors. Less well-developed are complete data pipelines that automate data storage, processing, and analysis (White et al. 2012). The result can be that slow manual collection of small amounts of data is replaced by slow manual management of large amounts of automatically-collected data. Therefore, what is needed is integrated HTP and data management systems incorporating both data acquisition and processing. Ideally, these systems would be sufficiently generic to be used with minimal or no alteration in both laboratory and field settings. We will present such a system in this and the chapters that follow, but first we will describe the biological system of interest.

The model plant *Arabidopsis thaliana*

The plant used as the test subject in this study is *Arabidopsis thaliana* (L.) Heynh. It is a small, rapidly maturing plant in the Brassicaceae that is native to Europe, Asia, and parts of North Africa. It has also invaded North America on several occasions and is, therefore, virtually

ubiquitous from latitude 25 to 65 N, except for Greenland. It is also found in parts of South America, Sub-Saharan Africa, Australia, and New Zealand. *Arabidopsis thaliana* is an important model system that has been used for identifying plant genes and determining their functions (Arabidopsis Genome Initiative, 2000). It has a small genome and its small stature and rapid development times make it an ideal genetic model plant for the same reasons that Drosophila is an ideal genetic model for animals. It was the first plant to have its genome sequenced (in 2000).

Figure 1.1 shows an *Arabidopsis* plant with key parts labeled. This study primarily focuses on vegetative development and the critical phenotypes are the areas, lengths, and angles of the rosette leaves, which form a circular pattern in close proximity to the ground.

Shade-avoidance responses

All plants are vulnerable to shading by taller neighbors and this is particularly so in Arabidopsis because its rosette is close to the ground. Shade-avoidance behaviors form a suite of responses that plants can undertake to find more light. They range from increased leaf elongation, alteration of leaf angles, growth in a more upward rather than outward direction, and even flowering more rapidly (Morelli and Ruberti 2000; Mullen et al. 2006).

Shade-avoidance responses are triggered by the reduced amounts of photosynthetically active radiation (PAR) transmitted through or reflected from plant tissues. In plant leaves, chlorophyll absorbs light more strongly in the red portion of the spectrum than in the longer-wavelength, far-red region (Smith, 1982). Phytochrome is an important plant pigment that has two molecular configurations that are differentially sensitive to these two wavebands; therefore, the plant is able to sense the ratio of red to far-red wavelengths (R: FR). Low ratios are an accurate signal of neighboring plant proximity and, therefore, a positive indicator of competitive intensity (Ballare et al. 1990; Smith et al. 1990; Gilbert et al. 2001; Schmitt et al. 2003). Thus,

shade-avoidance phenotypes constitute an interesting complex of traits whose intricate interactions with each other and with the environment are therefore widely studied (Weijschedé et al. 2006; Schmitt et al. 2003).

As listed above, leaf length, rosette area, and leaf angles are widely-studied traits related to shade-avoidance responses. Chitwood et al. (2012) manipulated far-red light to induce changes in leaf length. This study found a linear relationship between total leaf length and the square root of total leaf area. This study involved destructive sampling of fully-developed leaves. Studies of leaf angles are not only important in shade avoidance but also in studies of repetitive daily patterns of activity. Under some circumstances, plant leaves can rise and fall in an oscillatory behavior that can serve as a proxy for the cycling of the plant's circadian clock (Hong et al. 2013; Dornbusch et al. 2014). In indoor environments (although not in the field), *Arabidopsis* plants exhibit these nastic movements (Greenham et al. 2015).

In many shade-avoidance and growth-stage related studies, leaf area, leaf length and rosette area were obtained using mechanical measuring tools, such as calipers or rulers (Poethig and Sussex 1985; Boyes et al. 2001; Weijschedé et al. 2006, Gonzalez et al. 2010). The accuracy of those data, however, is limited by systematic error from the precision of conventional measuring tools along with human errors during invasive plant handling and subjective interpretation. The manual measurement process is also time-consuming and labor-intensive. Arvidsson et al. (2011) indicated a major bias in that the measurements of one stage during a particular plant developmental period are insufficient to interpret the phenotypes at other stages. Therefore, continuous time-series measurements during the entire developmental period are needed for studying shade-avoidance traits and, presumably, for other types of plant investigations as well.

Objectives

In the HTP pipeline to be described, the three traits of total leaf length, leaf area, and leaf angle will be detected by both 2D and 3D processing in a laboratory environment. The first two will also be monitored in the field using the 2D components of the same pipeline.

This pipeline is low-cost, fully-automated, and, as just noted, generic. That is, the pipeline was specifically designed at the application level to have cross-platform capabilities and a degree of instrument independence. As depicted by the flowchart shown in Figure 1.2, the pipeline contains five sections. 1) *Image data acquisition* used different platforms in indoor vs. field environments to collect time-series images of plant development. Indoor, stationary imaging systems were designed and mounted on each of six shelves in a growth chamber of University of California, Davis (UCD). At the University of Wyoming (UWY), a mobile imaging system was developed for use in the field. 2) *Image data storage, transmission, and management* involved the use of servers at UCD, UWY, and Kansas State University (KSU). For both the chamber and field experiments, images were stored locally and then transmitted via the iPlant Collaborative (http://www.iplantcollaborative.org/) (iPlant) to servers at KSU. This resulted in three complete backups of all image sets: one at the origin, one at iPlant, and one at KSU. 3) *Image processing* operations include pre-processing, orthophoto generation, and image segmentation. 4) *Metadata reconciliation* is necessary because metadata generated by different sources (i.e., human-entered data and/or some automated data) may conflict regarding the identity of each image. Reconciliation yields the most accurate pairings of genotype and phenotype data. 5) *Phenotype extraction* includes the machine-vision operations that yield the biological data that comprise the ultimate goal of the system. Python, a high-level scripting language, was used to connect and automate the sections.

In Chapter 2, we develop the pipeline in the context of a growth chamber experiment. It extracts data on total leaf length and 2D rosette area for a set of 1050 distinct *Arabidopsis* genetic lines comprising a nested association mapping (NAM) population. A NAM population is a set of plants specifically designed to permit measured traits to be associated with genomic regions by a particular form of statistical analysis (Brachi et al. 2010). Using the same pipeline, the relationship between these two traits will be analyzed both in the indoor environment where it was developed and also in the context of a field experiment using the same 1050 lines. This comparison will reveal how the pipeline is independent of the particular imaging platform used, as this is different for the two environments.

In Chapter 3, we used the same pipeline over time to extract hourly measurements of 2D rosette area under the indoor environment for analyzing plant growth and plant nastic movements across multiple diurnal cycles. In this context, "2D" means that the nastic movements were detected via the influence of leaf angle changes on apparent leaf lengths and areas. A shortcoming of the 2D approach is that there is no way to correct the length and area estimates to account for those movements; however, we then proceed to exploit 3D information to construct just a correction. The result is a novel system that is able to track both nastic movements and plant growth from the same images, something not previously possible.

References

Arabidopsis Genome Initiative, (2000). Analysis of the genome sequence of the flowering plant Arabidopsis thaliana, Nature, 408(6814), 796-815.

Arvidsson, S., Pérez-Rodríguez, P., & Mueller-Roeber, B. (2011). A growth phenotyping pipeline for Arabidopsis thaliana integrating image analysis and rosette area modeling for robust quantification of genotype effects. New Phytologist, 191(3), 895-907.

Ballare, C. L., Scopel, A. L., & Sanchez, R. A., 1990. Far-red radiation reflected from adjacent leaves: An early signal of competition in plant canopies. Science, 247 (4940), 329-332.

Bolon, Y. T., Haun, W. J., Xu, W. W., Grant, D., Stacey, M. G., Nelson, R. T., Gerhardt, D. J., Jeddeloh, J. A., Stacey, G., Muehlbauer, G. J., Orf, J. H., Naeve, S. L., Stupar, R. M., & Vance, C. P. (2011). Phenotypic and genomic analyses of a fast neutron mutant population resource in soybean. Plant physiology, 156(1), 240-253.

Bongaarts, J. (2014). United Nations, Department of Economic and Social Affairs, Population Division, Sex Differentials in Childhood Mortality. Population and Development Review, 40(2), 380-380.

Boyes, D. C., Zayed, A. M., Ascenzi, R., McCaskill, A. J., Hoffman, N. E., Davis, K. R., & Görlach, J. (2001). Growth stage–based phenotypic analysis of Arabidopsis a model for high throughput functional genomics in plants. The Plant Cell, 13(7), 1499-1510.

Blum, A., Mayer, J., & Gozlan, G. (1982). Infrared thermal sensing of plant canopies as a screening technique for dehydration avoidance in wheat. Field Crops Research, 5, 137-146.

Brachi, B., Faure, N., Horton, M., Flahauw, E., Vazquez, A., Nordborg, M., Bergelson, J., Cuguen, J., & Roux, F. (2010). Linkage and association mapping of Arabidopsis thaliana flowering time in nature. PLoS Genet, 6(5), e1000940.

Chen, D., Neumann, K., Friedel, S., Kilian, B., Chen, M., Altmann, T., & Klukas, C. (2014). Dissecting the Phenotypic Components of Crop Plant Growth and Drought Responses Based on High-Throughput Image Analysis. The Plant Cell, 26(12), 4636-4655.

Chitwood, D. H., Headland, L. R., Filiault, D. L., Kumar, R., Jiménez-Gómez, J. M., Schrager, A. V., Park, D. S., Peng, J., Sinha, N. R., & Maloof. J. N. (2012). Native environment modulates leaf size and response to simulated foliar shade across wild tomato species. PLoS One 7(1).

Dornbusch, T., Michaud, O., Xenarios, I., & Fankhauser, C. (2014). Differentially phased leaf growth and movements in Arabidopsis depend on coordinated circadian and light regulation. The Plant Cell Online, 26(10), 3911-3921.

Fiorani, F., & Schurr, U. (2013). Future scenarios for plant phenotyping. Annual review of plant biology, 64(2013), 267-291.

Furbank, R. T., & Tester, M. (2011). Phenomics–technologies to relieve the phenotyping bottleneck. Trends in plant science, 16(12), 635-644.

Gilbert, I. R., Jarvis, P. G., & Smith. H. (2001). Proximity signal and shade avoidance differences between early and late successional trees. Nature, 411(6839), 792-795.

Gonzalez, N., De Bodt, S., Sulpice, R., Jikumaru, Y., Chae, E., Dhondt, S., Van Daele, T., De Milde, L., Weigel, D., Kamiya, Y., Stitt, M., Beemster, G.T.S., Inzé, D. (2010). Increased leaf size: different means to an end. Plant Physiology, 153(3), 1261-1279.

Granier, C., Aguirrezabal, L., Chenu, K., Cookson, S. J., Dauzat, M., Hamard, P., Thioux, J., Rolland, G., Bouchier-Combaud, S., Lebaudy, A., Muller, B., Simonneau, T., & Tardieu, F. (2006). PHENOPSIS, an automated platform for reproducible phenotyping of plant responses to soil water deficit in Arabidopsis thaliana permitted the identification of an accession with low sensitivity to soil water deficit. New Phytologist, 169(3), 623-635.

Green, J. M., Appel, H., Rehrig, E. M., Harnsomburana, J., Chang, J. F., Balint-Kurti, P., & Shyu, C. R. (2012). PhenoPhyte: a flexible affordable method to quantify 2D phenotypes from imagery. Plant Methods, 8(1), 1-12.

Greenham, K., Lou, P., Remsen, S. E., Farid, H., & McClung, C. R. (2015). TRiP: Tracking Rhythms in Plants, an automated leaf movement analysis program for circadian period estimation. Plant methods, 11(1), 33.

Hong, S., Kim, S. A., Guerinot, M. L., & McClung, C. R. (2013). Reciprocal interaction of the circadian clock with the iron homeostasis network in Arabidopsis. Plant physiology, 161(2), 893-903.

Jansen, M., Gilmer, F., Biskup, B., Nagel, K. A., Rascher, U., Fischbach, A., Briem, S., Dreissen G., Tittmann, S., Braun, S., De Jaeger, I., Metzlaff, M., Schurr, U., Scharr, H., & Walter, A. (2009). Simultaneous phenotyping of leaf growth and chlorophyll fluorescence via GROWSCREEN FLUORO allows detection of stress tolerance in Arabidopsis thaliana and other rosette plants. Functional Plant Biology, 36(11), 902-914.

Morelli, G., & Ruberti, I. (2000). Shade avoidance responses. Driving auxin along lateral routes. Plant Physiology, 122(3), 621-626.

Mullen, J. L., Weinig, C., & Hangarter, R. P. (2006). Shade avoidance and the regulation of leaf inclination in Arabidopsis. Plant, Cell & Environment, 29(6), 1099-1106.

Poethig, R. S., & Sussex, I. M. (1985). The cellular parameters of leaf development in tobacco: a clonal analysis. Planta, 165(2), 170-184.

Schmitt, J., Stinchcombe, J. R., Heschel, M. S., & Huber, H. (2003). The adaptive evolution of plasticity: phytochrome-mediated shade avoidance responses. Integrative and Comparative Biology, 43(3), 459-469.

Smith, H. (1982). Light quality, photoreception, and plant strategy. Annual review of plant physiology 33(1), 481-518.

Smith, H., Casal, J. J., & Jackson, G. M. (1990). Reflection signals and the perception by phytochrome of the proximity of neighbouring vegetation. Plant, Cell & Environment, 13(1), 73-78.

Walter, A., Scharr, H., Gilmer, F., Zierer, R., Nagel, K. A., Ernst, M., Wiese, A., Virnich, O., Christ, M. M., Uhlig, B., Jünger, S., & Schurr, U. (2007). Dynamics of seedling growth acclimation towards altered light conditions can be quantified via GROWSCREEN: a setup and procedure designed for rapid optical phenotyping of different plant species. New Phytologist, 174(2), 447-455.

Wanscher, J. H. (1975). The history of Wilhelm Johannsen's genetical terms and concepts from the period 1903 to 1926. Centaurus, 19(2), 125-147.

Weijschedé, J., Martínková, J., De Kroon, H., & Huber, H. (2006). Shade avoidance in Trifolium repens: costs and benefits of plasticity in petiole length and leaf size. New Phytologist, 172(4), 655-666.

White, J. W., Andrade-Sanchez, P., Gore, M. A., Bronson, K. F., Coffelt, T. A., Conley, M. M., Feldmann, K. A., French, A. N., Heun, J. T., Hunsaker, D. J., Jenks, M. A., Kimball, B.

A., Roth, R. L., Strand, R. J., Thorp, K. R., Wall, G. W., & Wang, G. (2012). Field-based phenomics for plant genetics research. Field Crops Research, 133, 101-112.

Figure 1.1 Potted *Arabidopsis thaliana* plant.

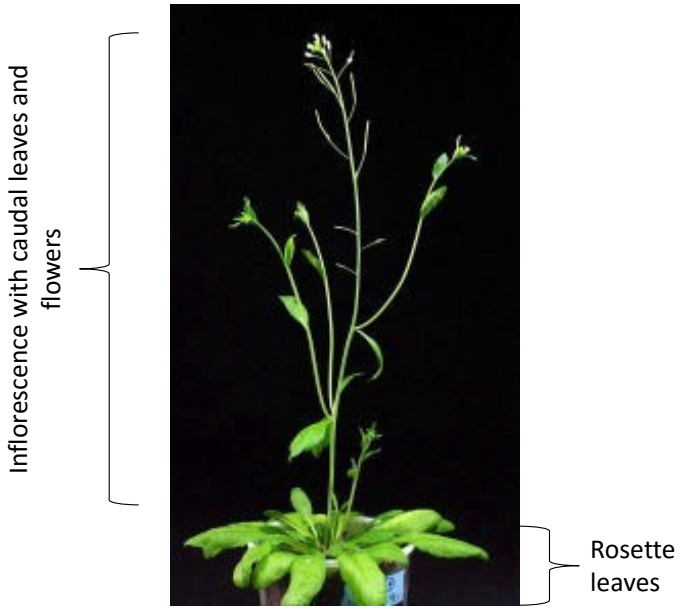

Figure 1.2. Flowchart of the high-throughput phenotyping pipeline.

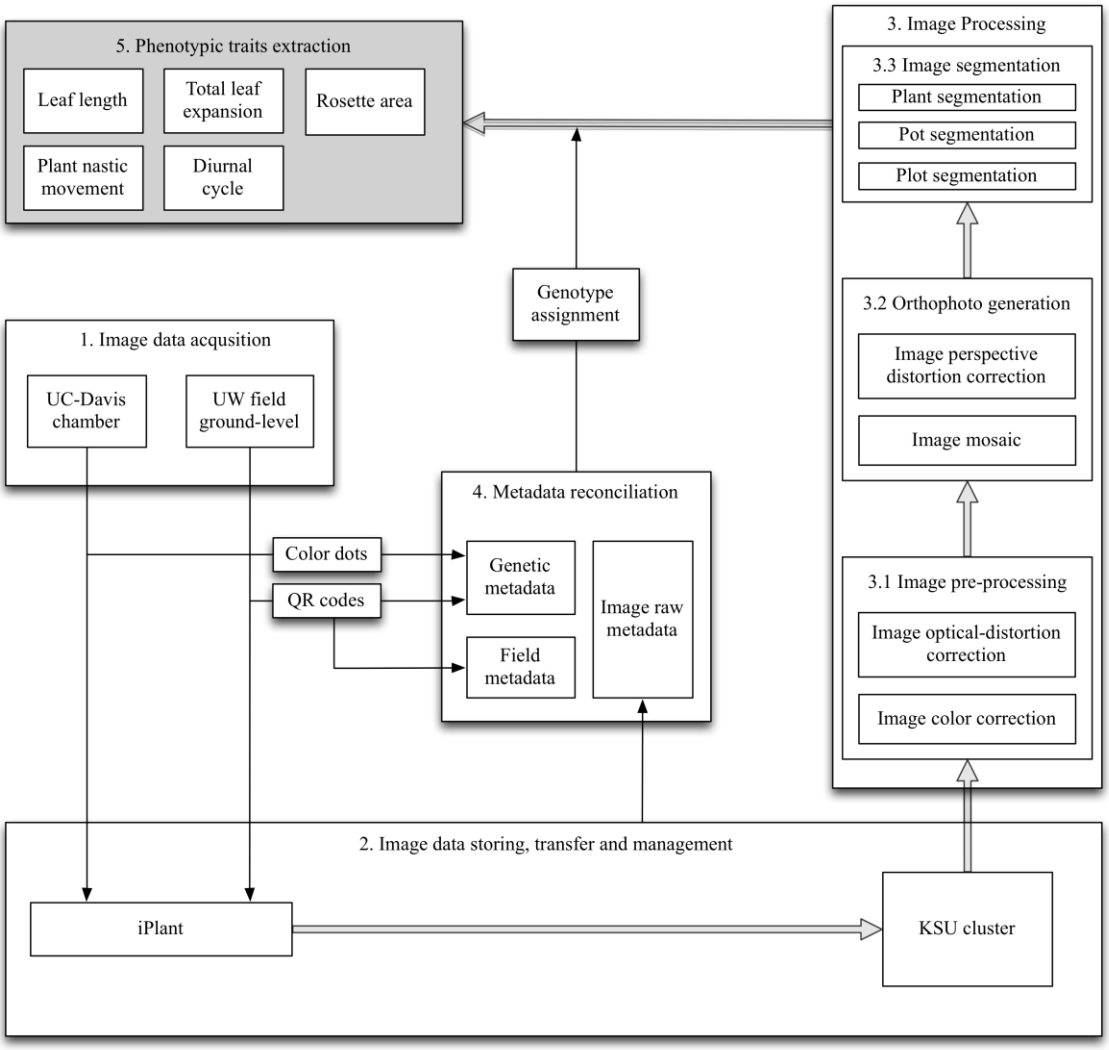

Chapter 2 - High-throughput phenotyping pipeline development

Introduction

Global crop production and plant biology is facing a tremendous challenge in that current production rates will not provide sufficient food to meet the demands of the world's population by 2050 (Bongaarts 2014). Previous studies (Furbank et al. 2009; Reynolds et al. 2009; Tester and Langridge 2010) showed that traditional breeding programs cannot sufficiently increase annual crop production for the three major cereal crops: rice, maize, and wheat. In the past decade, advances in gene technology, such as next generation DNA sequencing, have provided various means to improve plant breeding techniques. With these new techniques, breeders can potentially increase the rate of genetic improvement by molecular breeding (Phillips 2010).

Initial molecular genetics studies focused on studying *Arabidopsis thaliana* to gain an understanding of plants in general. O'Malley and Ecker (2010) reported that homozygous genome-wide knockout lines were available in *Arabidopsis thaliana*. Weigel and Mott (2009) stated that 1001 Arabidopsis ecotypes were sequenced to provide a comparative genomic database. Similarly, the genome sequences of many crops, such as rice, maize, wheat, sorghum, and barley, have also been obtained due to the dramatic reduction in sequencing costs in the past few years (Furbank and Tester 2011). Because of high-throughput genotyping, it is possible to develop large mapping populations and diversity panels for plant breeding (McMullen et al. 2009).

Although genotyping techniques have improved dramatically, methods of extracting phenotypic traits for large mapping populations are much less well-developed. This greatly limits our ability to quantitatively understand how genes relate to plant growth, environmental

adaptation, and yield. To remedy this, the genetic data need to be carefully and comprehensively linked to plant phenotypic traits in real-world environments (Miyao et al. 2007). In contrast to high-throughput genotyping that offers rapid and inexpensive genomic information extraction, conventional plant phenotyping methods are still labor-intensive and cost-inefficient. Plant phenotyping methods for smaller plants, such as *Arabidopsis*, are mainly dependent on intensive manual work for sampling, handling, and measuring plants often invasively, if not fully destructively. Due to this time-consuming process, very few phenotypic measurements can be acquired during the entire growing period (Arvidsson et al. 2011).

In the past few years, there has been increased interest in high-throughput phenotyping approaches in controlled indoor environments (Fiorani and Schurr 2013). These new approaches linking functional genomics, phenomics, and plant breeding are needed to improve both crop production and crop yield stability and also for efficient screening of high-yielding/stress-tolerant varieties (Bolon et al. 2011). Walter et al. (2007) and Jansen et al. (2009) used the GROWSCREEN/FLUORO system to measure chlorophyll and leaf counts. Granier et al. (2006) utilized the PHENOPSIS system to automate the soil water content control for screening soil water deficit response. Many studies (Furbank and Tester 2011; Dornbusch et al 2012; Green et al. 2012; Chen et al. 2014; Dornbusch et al. 2014) have used LemnaTec Scanalyzer HTS systems (http://www.lemnatec.com) to scan plant surfaces with imaging, laser systems to acquire and analyze plant images, or 3D point clouds for extracting certain phenotypic traits. The main advantage of the Scanalyzer HTS is that it is a fully-automated processing pipeline containing image acquisition, storage, management, and processing components, along with some subsequent statistical analyses of the resulting data.

Some larger-scale, fully-automated high-throughput phenotyping facilities have also been deployed in the greenhouses or growth chambers of private sector firms such as Monsanto and Dupont Pioneer and the most advanced national plant research institutions, such as the Australian Plant Phenomics Facility, the European Plant Phenotyping Network, and USDA. In these installations, robotics, precise environmental control, and remote sensing technologies are used to monitor and assess plant growth and development over time. Such high-end facilities require budgets far beyond those of most research laboratories, however, and may not be suitable for all situations, such as field environments.

To date, current field phenotyping approaches have mainly focused on automated solutions for data acquisition using platforms that integrate a vehicle, robotics, imaging systems, and sensors. Although this is changing, less work has been directed toward automating data storage, processing, and analysis. Due to these considerations and limitations, high-throughput phenotyping under field conditions has not yet reached its full potential.

Many previous indoor and field studies used imaging systems (cameras or scanners) and invasive sampling methods (excised plant parts) to extract phenotypic traits (Candela et al. 1999; Pérez-Pérez et al. 2002; Cookson et al. 2007; Bylesjö et al. 2008; Ali et al. 2012; Chitwood et al. 2012). These studies, however, failed to take into account the optical distortion generated by imaging system lenses and the perspective distortion created by the angle of view. True distances and areas cannot be determined from a 2D image if either optical distortion or perspective distortion are present, and merely facing the imagers straight down does not fix this problem. In particular, if a large number of plants are clustered for imaging, most of the plants will not be at the center of each individual frame. The plants on the corners of each frame will be distorted by the perspective viewing angle of the wide-angle lens (Figure 2.1). The optical distortion and

perspective distortion of the imaging system must therefore be removed before measuring any geometric quantities from a 2D image.

Therefore, in this chapter, we present a low-cost and fully-automated high-throughput imaging-based phenotyping pipeline suitable for both controlled environments and the field. This pipeline has three advantages compared to other existing pipelines: 1) a low-cost imaging system, 2) elements of instrument independency, and 3) cross-platform capability. The first advantage is that off-the-shelf, low-cost digital cameras were used as imaging devices instead of other possible remote sensors. This technique allows phenotypic traits (e.g., leaf length, rosette area, diurnal plant nastic movements, and plant vegetation conditions) to be extracted and measured directly from images.

The second advantage of this pipeline is a degree of instrument independency. For example, high-level scripts were used to interface with camera-manufacturer–supplied image processing software. Because many camera manufacturers provide similar tools, exchanging cameras becomes mainly a matter of altering the interface scripts.

The third advantage is cross-platform capability. Although the image data acquisition and data transfer methods may vary in different applications, the pipeline has a generic structure so that it can be deployed on different phenotyping platforms in multiple environments with minimal modification. Specifically, the pipeline was deployed on two different imaging platforms: a stationary growth chamber platform and a movable field platform. The novel, generic features enabling the pipeline to operate in these very different environments are outlined next.

In particular, the pipeline extracts plant phenotypic traits by: 1) removing image optical distortion and perspective distortion, and 2) applying mathematical algorithms to analyze rosette

parameters (e.g., rosette center, leaf tips) for total leaf expansion and 2D rosette area measurements. The workflow for image analysis and extracting rosette parameters from 2D images is shown in Figure 2.2.

Materials and methods

Imaging platform

Indoor imaging platform

The pipeline development was part of a growth chamber experiment conducted at University of California, Davis (UC-Davis) for studying the shade-avoidance response of an *Arabidopsis* NAM population. A total of 108 Canon Powershot S95 cameras were mounted facing straight down on six shelves—three shelves for simulating sun and three shelves for shade (Figure 2.3A and B). On each shelf, 18 cameras were mounted in a 2-row stationary camera frame 0.4-m height above the shelf surface. Each shelf held 24 (three rows of eight) 4-by-4 pot flats within a 0.80-by-2.13-m area.

Each camera was assigned a three-digit ID comprised of shelf number (1–6), row number (1–2), and camera position (1–9), in that order. Figure 2.3C is one individual image showing the field-of-view (FOV) of each camera and the color dot systems for tracking plant rotation. (The color-dot system is described below in the section on indoor genotype assignment.)

All of the cameras were set on manual focus, manual exposure mode (F7.1, 1/25 s, auto white balance), and a 28-mm (35-mm equivalent) focal length. A modified intervalometer script and the Canon Hack Development Kit (CHDK) firmware were installed on all of the cameras to trigger them simultaneously at the start of each hour. In order to prevent cameras from overheating, the LCD screen of each camera was turned off by this customized script after each

image was taken. All of the images were saved as Canon CR2 RAW format for preserving the maximal amount of geometric, spectral, and camera information.

Field imaging platform

The same genotypes of *Arabidopsis* used in the chamber were also planted outdoors at the University of Wyoming (UWY) Plant Science Station in Laramie. Plants were grown for a few days in biodegradable pots in the greenhouse and then transplanted to the field in a randomized block design. They were placed in a 10-cm grid with 14 rows and 6 columns. Two Canon EOS REBEL T3i DSLR cameras with Canon EF 20mm f/2.8 wide-angle lens were mounted on a moveable camera frame at a 95-cm height above the ground (Figure 2.4). Instead of facing straight down as in the chamber pipeline design, both cameras were mounted angled slightly towards each other to maximize the overlap area of their respective FOV.

For stability and repeatability, the camera mount was placed on a metal frame surrounding each plot. The inner frame dimensions were 153.0 cm by 73.6 cm. To image the whole plot, the camera mount was first moved to six fixed positions in sequence and pictures were taken. These six pairs did not fully capture all plants, but, because the cameras were on one side of the mount, a seventh position would only have seen the ground outside the plot. Therefore, the camera mount was turned 180 degrees and a final, seventh pair of pictures was taken.

Two Canon flashes with diffusers were attached on opposite sides of the camera mount. These served to limit the influence of the ambient light changes during the exposure interval and minimize camera mount shadows. Each flash was camera-controlled through an extension cable. Both cameras were set on manual focus, manual exposure mode (F9, 1/200 s, auto white balance). A customized camera trigger was built so both cameras fired simultaneously.

Image storing, management, and transfer

Indoor image storing, management, and transfer

All cameras were connected to a local data server at UC-Davis via USB cables for transferring images automatically. A Perl script written by Michael Covington renamed the hourly image files using the combination of the imaging date, time, and camera ID. Nighttime images were deleted and daytime (5:00 am to 8:00 pm) images were stored in the server. Although all of the 108 cameras were mounted in landscape orientation, the built-in auto rotation function of the cameras would sometimes rotate images to portrait orientation, creating problems in subsequent steps. To fix this, ExifTool (http://www.sno.phy.queensu.ca/~phil/exiftool/), a Perl-based program, was integrated into the pipeline to automatically rotate any RAW images found to be in portrait orientation. Each night, the pre-processed RAW images were transferred to a data store operated by the iPlant and, from there, to a server at KSU. Once the images reached the KSU server, they were organized into different subdirectories based on the imaging date, time, and shelf number. This set of transfers resulted in three redundant copies of the images being maintained at UC-Davis, iPlant, and KSU.

Field image storing, management, and transfer

For field image storing and transfer, images were first downloaded from the cameras onto a local computer at UW and then transferred to the data server at KSU via iPlant. Whereas the indoor system used camera IDs and dates to organize the images, QR codes containing block and plot numbers were employed in the field (Figure 2.5). The QR-code images were first automatically recognized within the stream of images by computing a color histogram and looking for a large number of white pixels. The images containing QR codes were converted to binary using a threshold that removed shadows, then ZBar (http://zbar.sourceforge.net/), a

freeware QR coder reader integrated into the pipeline, extracted the block number and plot number. This data was used to group the subsequent images into a directory named by image date, block, and plot information.

Missing camera detection mechanism of indoor imaging pipeline

During the imaging period, occasionally some cameras would accidently turn off, possibly due to unstable CHDK firmware. If not immediately detected and corrected, gaps in phenotypic data would result. Therefore, we included in the pipeline a mechanism for detecting missing cameras based on tracking the cameras' IDs in the image names. When missing camera IDs were detected, the pipeline automatically sent an email reporting the problem so it could be manually fixed.

Pipeline control

Agisoft Photoscan Pro (Photoscan), one of the programs to be described below, includes a Python scripting-capable application program interface (API) whose intent is to allow users to automate its capabilities. This was exploited to control all pipeline functions, including, in some cases, the control of programs completely external to Photoscan. The following sections describe all functions used in the processing pipeline, all of which were completely automated within the Photoscan Python API.

Image pre-processing

There were two corrections performed during the image pre-processing section for the images: image color correction and image optical distortion correction. The Canon Digital Photo Professional (DPP) program was used for color correction, optical distortion correction, and TIFF conversion.

Image color correction

Due to illumination variations across the shelf, the camera color responses differed slightly. For better plant segmentation process in the following step, the color of the RAW images was corrected by the white balance correction function of the DPP program. The spectral-lossless RAW file format was chosen despite its memory requirements to make this possible. Wide-angle lenses are also susceptible to vignetting effects where image brightness is reduced at the periphery. This can complicate color segmentation but was corrected during this process. A customized color-grid poster was photographed to verify the image color correction at the end of the process.

Image optical distortion correction

Few of the previous image-base phenotyping studies have considered lens distortion when extracting leaf parameters (length, width, and area). Due to the geometric distortion caused by lens optics, those leaf measurements have reduced accuracy for plants not at the center of each image. Using the RAW file format also allowed us to use manufacturer-provided lens profile data to correct the geometric distortion of each plant—another function built into DPP. After image color correction and optical distortion correction, TIFF image files were exported. The color-grid poster was also used for verifying the image optical distortion correction.

DPP automation

A design drawback of DPP is that it assumes a human will be using it to correct a small number of images. Thus, it lacks any automation capabilities. Therefore, AutoIt (https://www.autoitscript.com/site/autoit/), a BASIC-like scripting language, was used to automate the DPP graphical user interface (GUI). This language simulates user mouse clicks and text entries. While this may seem cumbersome, it is actually a major advantage of the pipeline.

Aside from the Perl script described, the AutoIt script is the only element of the pipeline that would have to be altered if a different brand of camera and manufacturer-provided image correction software were adopted.

Orthophoto generation

The final type of correction removed image perspective distortion. This was done by generating orthophotos, which are synthetic images produced as if each pixel is being viewed straight down. Thus, orthophotos permit geometric quantities such as 2D distances and areas to be measured with perspective effects removed. The Agisoft Photoscan Pro (Photoscan) program (http://www.agisoft.com) performed this step using the TIFF images output from DPP. This was done in nine-image subsets, each of which covered one half-shelf. (The original intent was to do full shelves but it was discovered after plants were added to the chamber that the vertical camera spacing did not permit this—a design flaw to be avoided in the future.) The program converted each set to an orthophoto. However, in the process of implementing this step, a subtle difference between the chamber and the field was uncovered that affected exactly how this should be done. This is described in the following two subsections.

Indoor environment image rendering method

Photoscan has four alternative rendering options for producing orthophotos: Mosaic, Average, Max Intensity, and Min Intensity. These govern the coloring method used to merge corresponding pixels from different images into the orthophoto. It was discovered that a wrong choice could have side effects for the small fraction of leaves that happened to have very different orientations with respect to different cameras. Specifically, the leaves would appear to be ghost-like double exposures. This was corrected by choosing the Mosaic method that favored

the camera whose view of ghost leaves was most vertical. An example orthophoto is shown as Figure 2.6A.

Field image rendering method

When used in the field, however, the Mosaic rendering method left pronounced shadows in the orthophoto that complicated subsequent processing steps. This was resolved by using the Average rendering method. This produces a more uniform orthophoto because areas that are shadowed by the camera mount in one image will often not be shadowed in others. Because it blends pixels, the Averaging method reduces shadow contrast.

To summarize the pipeline control description, Python scripts written and executed within Photoscan first invoke AutoIt to run a script in that language simulating user keystrokes and mouse clicks instructing DPP to remove lens and color distortion and produce TIFF formatted images. Once AutoIt processing is finished, the Python script then initiates Photoscan operations that produce the orthophoto. The same script then continues, executing the operations described in the following sections.

Image segmentation

Pot segmentation

In order to extract individual plants from each chamber orthophoto, the first step is to apply image segmentation to identify the pots. This was done using the following equation:

$$Pot = bw(Blue - Red),$$

where *Blue* is the pixel brightness value of the image blue channel, *Red* is the pixel brightness value of the image red channel, and *bw()* is the Otsu threshold method (Otsu 1975) for binary image transformation. Due to the slight illumination variation across each shelf, some of the pot

edges could not be detected. The probabilistic Hough Transformation (Duda and Hart 1972) was implemented in Python to identify the line segments and fill in the missing pot edges (Figure 2.6B). A 4-by-4 grid was generated for each flat based on the known dimensions of the pots and flats (Figure 2.6C).

Plant segmentation

Plant segmentation, the process of isolating the plants from other unwanted image features like soil, pots, or other items, is the next process applied to each orthophoto. The well-controlled illumination sources and image color corrections in the previous step allowed us to use a simple vegetation index for quick plant segmentation. The vegetation index used for this study computes the difference between the green and red channels and uses a ratio to normalize it throughout the entire imaging period. This measure, the Normalized Green–Red Difference Index (NGRDI) developed by Hunt et al. (2005), is similar to the well-known Normalized Difference Vegetation Index (NDVI). However, NDRDI is more useful to distinguish healthy vegetation from background in cameras like ours that have not been modified to be infrared-sensitive. The Otsu threshold method was then applied for transforming grayscale NGRDI images to a binary form in which the plant pixels are white and all non-plant pixels are black. The NDRDI equation in this study is as follows:

$$Plant = bw\left(\frac{Green - Red}{Green + Red}\right),$$

where *Green* is the pixel brightness value of the image green channel, *Red* is the pixel brightness value of the image red channel, and *bw()* is the Otsu threshold method for binary image transformation. The processed binary orthophoto is shown as Figure 2.6D. The NGRDI equation was implemented in Python and the Otsu threshold was from the Open Source Computer Vision Library (OpenCV; http://opencv.org/).

Plant genotype assignment

Indoor pipeline genotype assignment

Although growth chambers are well controlled, there are still temperature and lighting gradients that can affect plant growth and development. It is therefore common practice in *Arabidopsis* experiments to randomly reshuffle flats of pots every two to three days. Flat movements are recorded in spreadsheet form, but, to provide redundancy within the image data, a system using three-color dot combinations on each flat was developed. A color-dot detection and decoding routine was integrated into the processing pipeline for automatically tracking pots so that the proper genotypes of each plant could be paired with the ultimate measured phenotypes.

Field pipeline genotype assignment

Because all of the plants were placed with a 14-by-6 planting grid in each plot of the field study, a Python routine was integrated in the pipeline to generate a 14-by-6 grid on each plot orthophoto for extracting plants. However, due to some irregularities of planting grid placement in each plot, each plot orthophoto needed to be cropped first so the grids were generated in appropriate positions (Figure 2.7). As each plant was extracted, plant position and QR-code data on block and plot number was used to rename each single-rosette image. This information was paired with the genotype metadata collected when plant locations were assigned.

Phenotypic traits extraction

Leaf length and total leaf expansion calculation

The key step in measuring leaf length is the detection of the rosette center and leaf tips on each single-rosette binary image. The contours of each binary image were analyzed first and the

image moments were then calculated (https://en.wikipedia.org/wiki/Image_moment). The rosette center was estimated using the binary image centroid of all white (i.e., plant) pixels. That is:

$$(\bar{x}, \bar{y}) = \left(\frac{M_{10}}{M_{00}}, \frac{M_{01}}{M_{00}}\right),$$

where $\bar{x}$ and $\bar{y}$ are the coordinates of the binary image centroid and *M* are image moments.

Using the calculated rosette center as the origin, a radial scan was executed on the binary image to yield a curve representing the traced rosette outline in a 2D plot. The leaf tips, the points most distant from the plant center, should be the peaks of the curve just described. However, at first it was challenging to find accurate peak locations due to the rough edges of plant leaves. This was even more complicated when parts of the leaves appeared to be missing due to damage or segmentation faults. Therefore, the rosette-outline curve was first smoothed using Savitzky–Golay filter (Savitzky and Golay 1964) so small, erroneous maxima could be removed. The next step was to fit a Chebyshev polynomial (Tchebychev, 1853) to the smoothed rosette-outline curve. Putative peaks were then located by calculating the roots (i.e., zeros) of the first derivative of the Chebyshev polynomial curve. Unfortunately, this procedure still yielded false leaf tip positions sometimes.

Therefore, as a second step, the peak widths were analyzed using the x coordinates of the rosette-outline curve to find the minimum peak width, which was used as the length of a moving window centered at each detected curve peak. Within this moving window, the maximum of the fitted rosette-outline curve and the maximum of the original rosette-outline curve were compared. The true peak locations were recovered if the maximum of the original rosette-outline curve was higher. The pixel coordinates of the leaf tips were calculated based on the curve peak locations. The length of each leaf was measured as the distance from the rosette center to the leaf tip. The total leaf expansion of each plant is the sum of all of the leaf lengths.

Rosette area calculation

The rosette area in each single-rosette binary image can be simply calculated by computing the total number of white pixels in each single-rosette binary image.

Statistical modeling

Chitwood et al. (2012) manipulated far-red light to induce changes in leaf length as an index of the shade-avoidance response. This study demonstrated a linear relationship between total leaf length and square root of the total leaf area. To test the relationship between total leaf expansion and rosette area using our workflow, we implemented the power law function to fit the phenotype data with the following equation:

$$Total\ Leaf\ Expansion = a * \ Rosette\ Area^{b},$$

where *a* and *b* are parameters that determine the trajectory and shape of the power law function, respectively.

The parameters *a* and *b* were estimated using the Levenberg-Marquardt non-linear least square method. Bootstrap resampling was used to calculate 95% confidence intervals (CI) based on 10000 simulations. The power law function and the least square estimation were implemented using Python Scipy package.

Indoor pipeline data analysis

Data for total leaf expansion and rosette area measured on four different dates during a 10-day growth period were used for the analysis. The first set of data was collected the eighth day after plant emergence, followed by three subsequent datasets at two-day intervals. The time points of this test were selected so that: 1) the plants were big enough to distinguish individual leaves from the start, 2) the final image had a large rosette, and 3) leaf overlap areas between

adjacent plants were minimal. All of the images from the indoor pipeline were taken at 6:00 am to minimize any possible ambient influences.

Field pipeline data analysis

The same genotypes tested in the indoor environment were also tested in the field experiment. Data from six different days were used to fit the same relationship. They were selected from an 18-day period in which Day 1 was the third day after plants were transplanted in the field. Five subsequent dates, each three to four days apart, followed. (The dates of field image data collection were dependent on weather conditions.)

Results and discussion

Indoor imaging pipeline throughput capability

Because there was a certain amount of unavoidable manual work during image acquisition in the field, the completely-automated indoor pipeline was used to evaluate the throughput capability of the phenotyping pipeline.

Orthophoto generation, which initially required 38 CPU-minutes per half-shelf, was the most time-consuming process in the entire pipeline. By implementing High Performance Computing (HPC) routines using OpenCL and AMD GPUs in the pipeline, this processing time was reduced to 25 minutes per half-shelf orthophoto. These HPC routines were also utilized in other steps. It took approximately 6–8 minutes to detect pots and decode the color dots for genotype assignment, then two minutes for extracting phenotypic trait data (e.g., total leaf expansion, rosette area). Therefore, the total runtime of the entire processing pipeline was 35 minutes maximum for each half-shelf.

The second method for improving pipeline throughput was to use distributed parallel computing routines to spread the processing tasks across a small computing cluster. Two split

half-shelf orthophotos from each shelf were processed by two nodes simultaneously. For the chamber application, there were 24 4-by-4 pot flats on each of the six shelves, which made 2,304 plants photographed hourly. Because imaging was conducted for 16 hours per day, a total of 36,864 single-plant pictures were obtained each day. Each cluster node processed 192 plant images in 35 minutes, equating to at least five plants per minute. Therefore, the runtime for processing 16 hours of single-rosette images on the six-node cluster was 11.2 hours. The capabilities of the chamber processing pipeline are shown in Table 2.1.

This pipeline was fast because all 108 cameras took images for six shelves simultaneously. The times for image storing, management, and transfer have not been included in this analysis because of variations in local network and internet speeds. In the future, when the processing pipeline is executed on a local computer cluster at UC-Davis for minimizing data transfer time, all 2,304 plants can be screened within an hour.

Image analysis

Image optical distortion and color correction

The 28-mm (35-mm equivalent) focal length caused the optical distortion to be much more severe on the image edges than on the image center. Figure 2.8A shows the color-grid image before optical distortion removal. The red reference line was drawn on the image to illustrate the curvature of the color grids caused by the optical distortion. Using Canon DPP to remove optical distortion was accurate and efficient because of the manufacturer's lens profile database. Figure 2.8B shows that the curvature of the edges of color grids was removed after the optical distortion correction. The red reference line matched the edge of the color grid.

Due to variations in shelf illumination and camera firmware differences, the original images were greener than the original RGB values of color grids. After comparing different

image color correction packages, the Canon DPP software provided reasonably accurate color correction using the white balance function provided by the camera manufacturer. After color correction, the green tone was removed and the photographed RGB values were very close to the original (Figure 2.9).

Image perspective distortion correction

Figure 2.10 (A–B) shows two plants at the corner of the individual frame. The effects of perspective are clear because a great deal of pot wall can be seen compared to plants at the image centers, where much less wall is visible. Due to this issue, direct measurements from the image centers and corners are not comparable; Figure 2.10 (C–D) shows that after re-projecting each pixel vertically. The sidewalls of the pots were largely corrected and only a small portion of the pots' sidewalls were visible compared to the uncorrected images. Moreover, the red-box–highlighted leaves showed more leaf area in the corrected image for both of the plants when the leaves were not entirely flat. The two pots shown in Figure 2.10 are from the most extreme corners of the shelf, so the small portions of visible sidewalls are inevitable. For most of the pots, the sidewalls were well corrected.

Moreover, the blue-box–highlighted leaves show that leaf positions were also corrected. For plant 1 (Figure 2.10A), the two leaves in the blue box showed a side-by-side position, but in reality, the smaller leaf was under the big leaf, as the corrected image shows (Figure 2.10C). For plant 2, the two leaves highlighted by blue boxes overlapped in the uncorrected image but distinguished clearly after correction (Figure 2.10B and 2.10D). Although smaller leaves could not be counted when covered by bigger leaves, the perspective-distortion–corrected images will provide more accurate leaf length and rosette area measurements, which are more critical when studying leaf shade-avoidance responses.

Rendering methods for indoor and field orthophoto

Most previous studies did not use orthophotos for extracting phenotypic traits from 2D images and therefore did not have occasion to compare rendering methods. In the chamber, each plant appeared in two views, one necessarily more oblique than the other. In a small number of cases, the leaf angles were sufficiently extreme that, depending on how the orthophoto was rendered, a double image of the leaf would result. Figure 2.11 illustrates the double image problem and how it was resolved using the Mosaic method, which colors the orthophoto using the image pixels that resolve as being closest in 3D space.

The red-box–highlighted leaves in Figure 2.11A and B were photographed with different viewing angles by adjacent cameras 514 and 515. In this instance, a small leaf was covered by a bigger leaf. Camera 515 photographed them at an oblique angle so both leaves were visible to this camera but not to Camera 514. Because of this, under the Average rendering method, which blends corresponding pixel colors from both images, the highlighted leaf appears twice in the orthophoto (Figure 2.11C). This defect would subsequently confuse the leaf tip detection algorithm. However, in Figure 2.11D, when the Mosaic rendering method was used, the plant outline was not confusing and the "double-leaf" issue was solved.

There are actually three defects in Figure 2.11 which need to be discussed: one is partial overlap (top red box), one is different viewing angle (middle red box), and the last is complete overlap (bottom red box). With the Average method, all three create spurious leaf tips due to differences in the "opacity" of the double images. However, the Mosaic method fixes this issue at the cost of occasionally losing an entire leaf (bottom red box).

On the other hand, in the field environment, the two cameras were relatively far away from the plants, so the viewing-angle issue was not as pronounced as in the chamber. Instead, the

major problem affecting rendering was the strong ambient illumination by sunlight, which cast constantly-changing shadows of the camera mounts into the plots. Originally, it was thought that the flashes could be used to completely eliminate shadows. Unfortunately, this required their most powerful settings, which saturated image brightness. Therefore, a lower setting was used in combination with the Average rendering method to improve the consistency of the brightness of the orthophoto. Figure 2.12A shows pronounced camera mount shadows when the Mosaic rendering method was used. Subsequent image segmenting by color analysis was not able to achieve equal results at identifying plants under shadowed and non-shadowed conditions. However, in Figure 2.12B, the orthophoto produced by the Average rendering method shows more uniform brightness throughout the entire plot. These images could be successfully segmented even though the shadows were not completely eliminated.

Field QR codes imaging and processing

QR codes provided a very efficient way to store plot metadata and organize plot images. Initially, the ground-level field pipeline could successfully recognize all of the QR-code images among other field images by analyzing the histograms of the images, but there were some failed attempts when the ZBar reader tried to decode the QR codes. The failed attempts occurred when the shadow of the camera mount fell on the QR codes. To solve this issue, the brightness and contrast of all of the recognized QR-code images were first increased to minimize the shadow, then the adjusted images were thresholded to a shadow-free binary image. With this improvement, all of the QR codes were successfully decoded and the plot metadata was accurately extracted.

Leaf tip detection refinement

Accurate leaf tip detection is critical to measuring leaf length and total leaf length expansion. Initially, however, many false leaf tips were detected, due to small irregularities on the original rosette-outline curve (Figure 2.13). As Figure 2.14 shows, the estimated peak locations were shifted from the original rosette-outline curve peak locations, and peak heights were lowered due to smoothing after the Savitzky–Golay filter and the Chebyshev Polynomial curve fitting. However, after the second iteration of the leaf tip detection, most of the peak locations from the first iteration were shifted back to the original radial-scan-yield curve peak locations, true peak locations were recovered, and many false peaks were eliminated. These optimization operations provide much more accurate rosette-outline peaks for positioning the true leaf tips on the single-rosette binary image. This method was especially accurate and efficient for finding the leaf tips when the leaves were damaged, as in the example in Figure 2.14.

Relationship between rosette area and total leaf expansion

Relationship for indoor pipeline

The estimated parameter *b* of the power law function from Day 1 to Day 4 is 0.836 (Figure 2.15A), 0.753 (Figure 2.15B), 0.750 (Figure 2.15C), and 0.636 (Figure 2.15D), respectively, indicating a change in shape from near-linearity to a more curved relationship. The range of possible estimates for parameters *a* and *b* obtained from 10000 bootstrap simulations is shown in Figure 2.16. The histograms shows the frequency of estimate for *a* and *b* in 10 bins. The mean, median, and mode for *a* and *b*, respectively, are very close to the original estimate from the least squares fit. The analyses of the parameter distributions and the bootstrap 95% confidence intervals are shown in Table 2.2.

Because the confidence limits for Days 1 and 4 do not overlap, it can be said that the exponent of the power law decreases with time while the slope factor increases, although there is considerable uncertainty about the values of parameter *a*. However, the range of values for *b* is within the reasonable expectations of being not greater than 1 and not less than 0.5. These values are consistent with the idea young leaves mainly grow by elongation. However, in later developmental stages, total leaf expansion slows relative to leaf-width growth increases, which become the main contributor to increasing rosette area. Chitwood et al. (2012) reported a linear relationship between total leaf length and square root of the total leaf area (i.e., b=0.5*)* for tomato leaves at a late developmental stage. This result is very similar to our finding of b=0.636 during late development.

This dynamic relationship between total leaf expansion and rosette area has not been reported previously, quite possibly because destructive sampling made it impossible to collect time-series data from the same plant during growth. Our non-invasive imaging method, however, can be used to track the time-series development pattern for single plants in a mapping population.

Relationship for field pipeline

The estimated parameters *a* and *b* and the power law curves for Days 1 to 6 in the field are shown in Table 2.3 and Figure 2.17A-F, respectively. The *b* values also followed a descending trend over time. Figure 2.18 shows the analyses of the parameter distributions and the bootstrap 95% confidence intervals. This result follows what is seen in the chamber; that is, *b* is close to 1 at the beginning of the growth period but decreases over time. As above, the confidence intervals of the first and last days do not overlap, showing that *a* increases with time

and *b* falls. Again, *b* showed the pattern of being close to 1 earlier and not less than 0.5 later. This also appears similar to the Chitwood et al. (2012) result.

It is noticeable that the *b* value increased at Day 6, mainly because of a highlight outlier. The Figure 2.17G shows that this outlier was from a bolting plant that yielded a confusing single-rosette binary image. The center part of this binary was missing due to bolting, and a noisy plant outline caused falsely-detected leaf tips (Figure 2.19). After removing this outlier, the *b* value dropped to 0.749.

It is possible the parameter *b* would keep decreasing if a few more time points could be used. However, from Day 6, many genotypes started bolting, which created difficulties in generating clean binary images and deceased the reliability of the total leaf expansion and rosette area measurements.

Conclusion and perspectives

We presented a low-cost, versatile, and automated high-throughput phenotyping pipeline based on imaging technology to extract plant phenotypic traits under different environmental conditions. Our pipeline integrated a series of automated operations, including: image data acquisition in a controlled indoor environment, image data transfer and management, genotype assignment, phenotypic trait extraction, and analytical processes. The field image data acquisition was not fully automated due to different experimental designs compared to the indoor environment.

Our HTP pipeline dealt with many photogrammetric issues that have not been previously considered in most biology studies. Images were first processed for optical and perspective distortion removal to make sure the true geometric quantities (e.g., distance and area) could be measured based on 2D images. Next, mosaicked orthophotos of each shelf were created hourly

for a mapping population. Last, segmented single-rosette images were extracted from the orthophotos for measuring leaf length and rosette area with our novel image processing algorithm. This method transforms computing-expensive image processing operations to mathematical curve fitting problems and provides a reliable solution for leaf tip detection in the face of leaf irregularities, segmentation errors, and damage.

With this framework of phenotyping, time-series phenotypic traits of a mapping population can be extracted and analyzed in a short period of time. In this study, we found a power-law correlation between total leaf expansion and rosette area from our time-series analysis. At the early developmental stage, this relationship was close to linear; towards the end of the developmental stages, the exponent started decreasing. The late-stage finding is very similar to the results reported by Chitwood et al. (2012).

There are still some aspects of this pipeline that need to be improved for future work. The color-dot system of chamber study was used to track flat position and orientation changes in the orthophoto. However, the QR-code approach proved its robustness and feasibility for storing metadata and could be competitive in chamber settings to enable genotype assignment. Moreover, aerial-level field studies could also use QR-code system to store crop variety or field position metadata.

Acknowledgement

This study was funded by the National Science Foundation Grant IOS-0923752 to Cynthia Weinig, Stephen Welch, Julin Maloof, and C. Robertson McClung. We want to thank Christine Palmer (UC-Davis), Robert Baker (UWY), Cody Markelz (UC-Davis), James Ta (UC-Davis), Smita Sharan (KSU), Rishab Vaswani (KSU), Lakshmi Narjala (KSU), Wen Fung Leong

(KSU), Huan Wang (KSU), and Siben Li (University of Edinburgh) for providing valuable suggestions on modeling and statistics. We are also appreciative of the helpful comments and suggestions of reviewers.

References

Ali, M. M., Al-Ani, A., Eamus, D., & Tan, D. K. (2012). A New Image-Processing-Based Technique for Measuring Leaf Dimensions. American-Eurasian Journal of Agriculture & Environmental Science, 12, 1588-1594.

Arvidsson, S., Pérez-Rodríguez, P., & Mueller-Roeber, B. (2011). A growth phenotyping pipeline for Arabidopsis thaliana integrating image analysis and rosette area modeling for robust quantification of genotype effects. New Phytologist, 191(3), 895-907.

Bolon, Y. T., Haun, W. J., Xu, W. W., Grant, D., Stacey, M. G., Nelson, R. T., Gerhardt, D. J., Jeddeloh, J. A., Stacey, G., Muehlbauer, G. J., Orf, J. H., Naeve, S. L., Stupar, R. M., Vance, C. P. (2011). Phenotypic and genomic analyses of a fast neutron mutant population resource in soybean. Plant physiology, 156(1), 240-253.

Bongaarts, J. (2014). United Nations, Department of Economic and Social Affairs, Population Division, Sex Differentials in Childhood Mortality. Population and Development Review, 40(2), 380-380.

Bylesjö, M., Segura, V., Soolanayakanahally, R. Y., Rae, A. M., Trygg, J., Gustafsson, P., Jansson, S., Street. N. R. (2008). LAMINA: a tool for rapid quantification of leaf size and shape parameters. BMC Plant Biology, 8(1), 82.

Candela, H., Martınez-Laborda, A., & Micol, J. L. (1999). Venation pattern formation in Arabidopsis thaliana vegetative leaves. Developmental biology, 205(1), 205-216.

Chen, D., Neumann, K., Friedel, S., Kilian, B., Chen, M., Altmann, T., & Klukas, C. (2014). Dissecting the phenotypic components of crop plant growth and drought responses based on high-throughput image analysis. The Plant Cell, 26(12), 4636-4655.

Chitwood, D. H., Headland, L. R., Filiault, D. L., Kumar, R., Jiménez-Gómez, J. M., Schrager, A. V., Park, D. S., Peng, J., Sinha, N. R., Maloof. J. N. (2012). Native environment modulates leaf size and response to simulated foliar shade across wild tomato species. PLoS One, 7(1).

Cookson, S. J., Chenu, K., & Granier, C. (2007). Day length affects the dynamics of leaf expansion and cellular development in Arabidopsis thaliana partially through floral transition timing. Annals of Botany, 99(4), 703-711.

Dornbusch, T., Lorrain, S., Kuznetsov, D., Fortier, A., Liechti, R., Xenarios, I., & Fankhauser, C. (2012). Measuring the diurnal pattern of leaf hyponasty and growth in Arabidopsis–a novel phenotyping approach using laser scanning. Functional Plant Biology, 39(11), 860-869.

Dornbusch, T., Michaud, O., Xenarios, I., & Fankhauser, C. (2014). Differentially phased leaf growth and movements in Arabidopsis depend on coordinated circadian and light regulation. The Plant Cell, 26(10), 3911-3921.

Duda, R. O., & Hart, P. E. (1972). Use of the Hough transformation to detect lines and curves in pictures. Communications of the ACM, 15(1), 11-15.

Fiorani, F., & Schurr, U. (2013). Future scenarios for plant phenotyping. Annual review of plant biology, 64, 267-291.

Furbank, R. T., von Caemmerer, S., Sheehy, J., & Edwards, G. (2009). C4 rice: a challenge for plant phenomics. Functional Plant Biology, 36(11), 845-856.

Furbank, R. T., & Tester, M. (2011). Phenomics–technologies to relieve the phenotyping bottleneck. Trends in plant science, 16(12), 635-644.

Granier, C., Aguirrezabal, L., Chenu, K., Cookson, S. J., Dauzat, M., Hamard, P., Thioux, J., Rolland, G., Bouchier-Combaud, S., Lebaudy, A., Muller, B., Simonneau, T., Tardieu, F. (2006). PHENOPSIS, an automated platform for reproducible phenotyping of plant responses to soil water deficit in Arabidopsis thaliana permitted the identification of an accession with low sensitivity to soil water deficit. New Phytologist, 169(3), 623-635.

Green, J. M., Appel, H., Rehrig, E. M., Harnsomburana, J., Chang, J. F., Balint-Kurti, P., & Shyu, C. R. (2012). PhenoPhyte: a flexible affordable method to quantify 2D phenotypes from imagery. Plant Methods, 8(1), 1-12.

Hunt Jr, E. R., Cavigelli, M., Daughtry, C. S., Mcmurtrey III, J. E., & Walthall, C. L. (2005). Evaluation of digital photography from model aircraft for remote sensing of crop biomass and nitrogen status. Precision Agriculture, 6(4), 359-378.

Jansen, M., Gilmer, F., Biskup, B., Nagel, K. A., Rascher, U., Fischbach, A., Briem, S., Dreissen G., Tittmann, S., Braun, S., De Jaeger, I., Metzlaff, M., Schurr, U., Scharr, H., Walter, A., 2009. Simultaneous phenotyping of leaf growth and chlorophyll fluorescence via GROWSCREEN FLUORO allows detection of stress tolerance in Arabidopsis thaliana and other rosette plants. Functional Plant Biology 36, 902-914.

McMullen, M.D., Kresovich, S., Villeda, H.S., Bradbury, P., Li, H., Sun, Q., Flint-Garcia, S., Thornsberry, J., Acharya, C., Bottoms, C. (2009). Simultaneous phenotyping of leaf growth and chlorophyll fluorescence via GROWSCREEN FLUORO allows detection of stress tolerance in Arabidopsis thaliana and other rosette plants. Functional Plant Biology, 36(11), 902-914.

Miyao, A., Iwasaki, Y., Kitano, H., Itoh, J., Maekawa, M., Murata, K., Yatou, O., Nagato, Y., Hirochika. H. (2007). A large-scale collection of phenotypic data describing an

insertional mutant population to facilitate functional analysis of rice genes. Plant molecular biology, 63(5), 625-635.

O'Malley, R. C., & Ecker, J. R. (2010). Linking genotype to phenotype using the Arabidopsis unimutant collection. The Plant Journal, 61(6), 928-940.

Otsu, N. (1975). A threshold selection method from gray-level histograms. Automatica, 11(285-296), 23-27.

Pérez-Pérez, J. M., Serrano-Cartagena, J., & Micol, J. L. (2002). Genetic analysis of natural variations in the architecture of Arabidopsis thaliana vegetative leaves. Genetics, 162(2), 893-915.

Phillips, R. L. (2010). Mobilizing science to break yield barriers. Crop Science, 50, S-99–S-108.

Reynolds, M., Foulkes, M. J., Slafer, G. A., Berry, P., Parry, M. A., Snape, J. W., & Angus, W. J. (2009). Raising yield potential in wheat. Journal of Experimental Botany, erp016.

Savitzky, A., & Golay, M. J. (1964). Smoothing and differentiation of data by simplified least squares procedures. Analytical chemistry, 36(8), 1627-1639.

Tchebychev, P. L. (1853). Théorie des mécanismes connus sous le nom de parallélogrammes. Imprimerie de l'Académie impériale des sciences.

Tester, M., & Langridge, P. (2010). Breeding technologies to increase crop production in a changing world. Science, 327(5967), 818-822.

Walter, A., Scharr, H., Gilmer, F., Zierer, R., Nagel, K. A., Ernst, M., Wiese, A., Virnich, O., Christ, M.M., Uhlig, B., Jünger, S., Schurr, U. (2007). Dynamics of seedling growth acclimation towards altered light conditions can be quantified via GROWSCREEN: a setup and procedure designed for rapid optical phenotyping of different plant species. New Phytologist, 174(2), 447-455.

Weigel, D., & Mott, R. (2009). The 1001 genomes project for Arabidopsis thaliana. Genome Biol, 10(5), 107.

Figure 2.1 Original image with optical distortion and perspective distortion.

An original image from indoor environment showing plants before optical distortion and perspective distortion correction. The plants from the corners were seriously distorted and the true distance and area cannot be measured directly from the image.

Figure 2.2 Image analysis workflow.

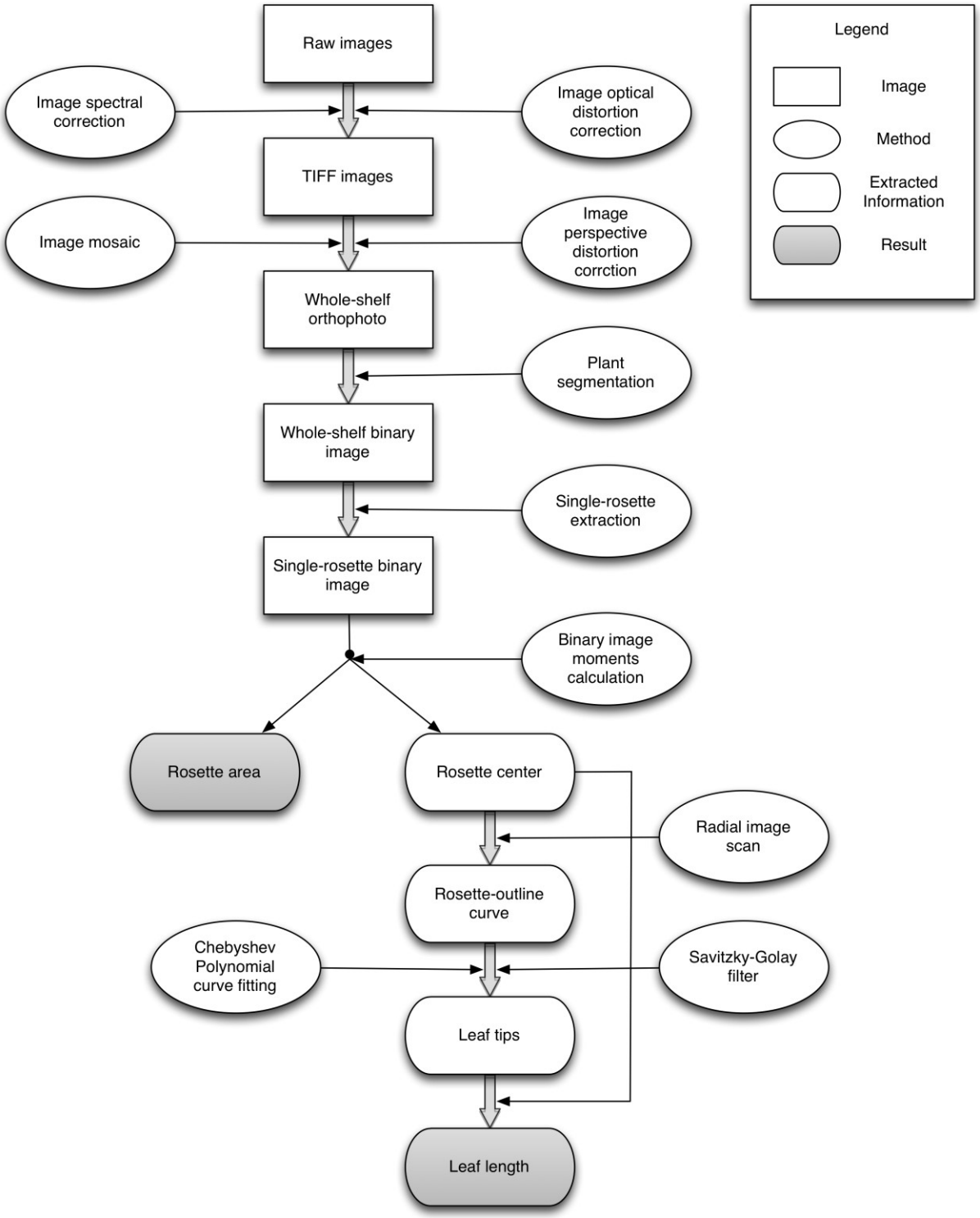

Figure 2.3 Indoor imaging platform.

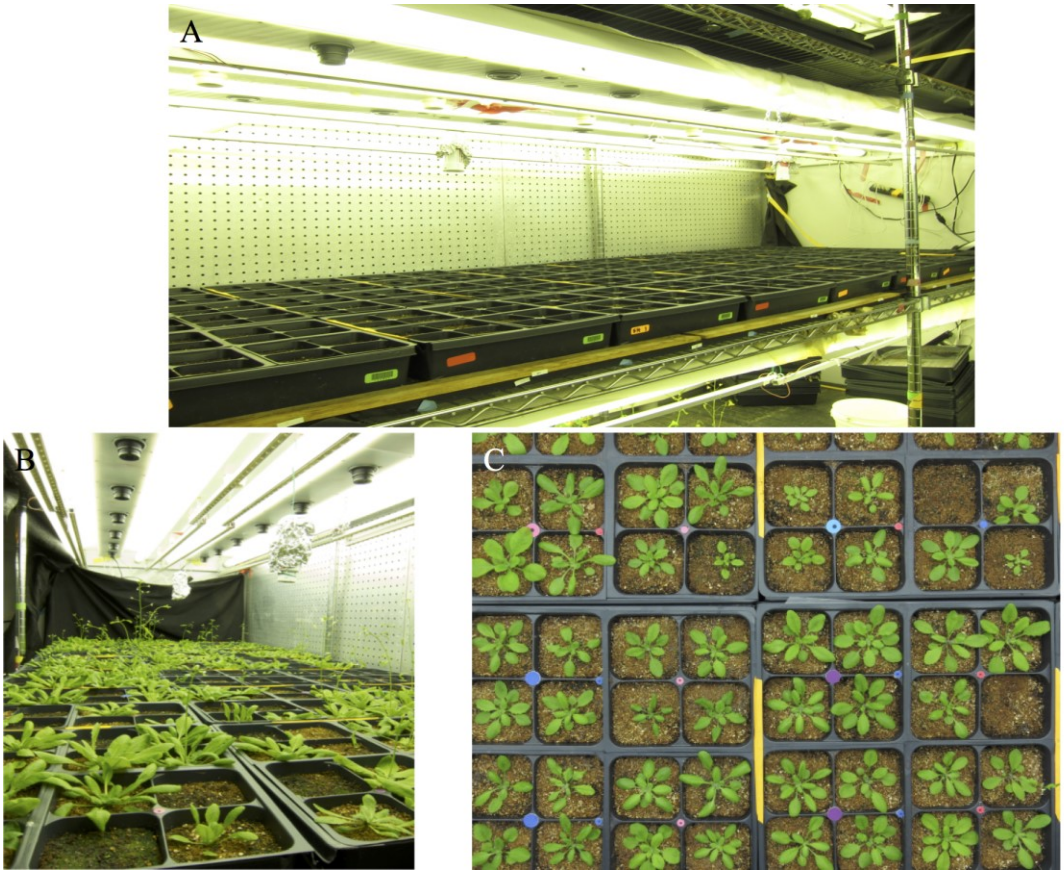

A and B show the chamber imaging system on each shelf. C is an individual image from one camera. The color-dot system was used to track 4-by-4 pot flat rotation during the growing period.

Figure 2.4 Field imaging platform.

The ground-level field imaging setup. Two Canon DSLR cameras were mounted with an angle. Two flashes with diffusers were mounted on the side bars for creating a uniform illumination condition.

Figure 2.5 Field image data management.

Three successive images from one camera. Left to right they are: the last image from the preceding plot, the first image from the next plot with a QR code held in the camera view, and the same plot view with the QR code removed. The image containing the QR code is recognized by its large number of white pixels. The QR code is then read to identify the new plot and the block that contains it.

Figure 2.6 Orthophoto processing.

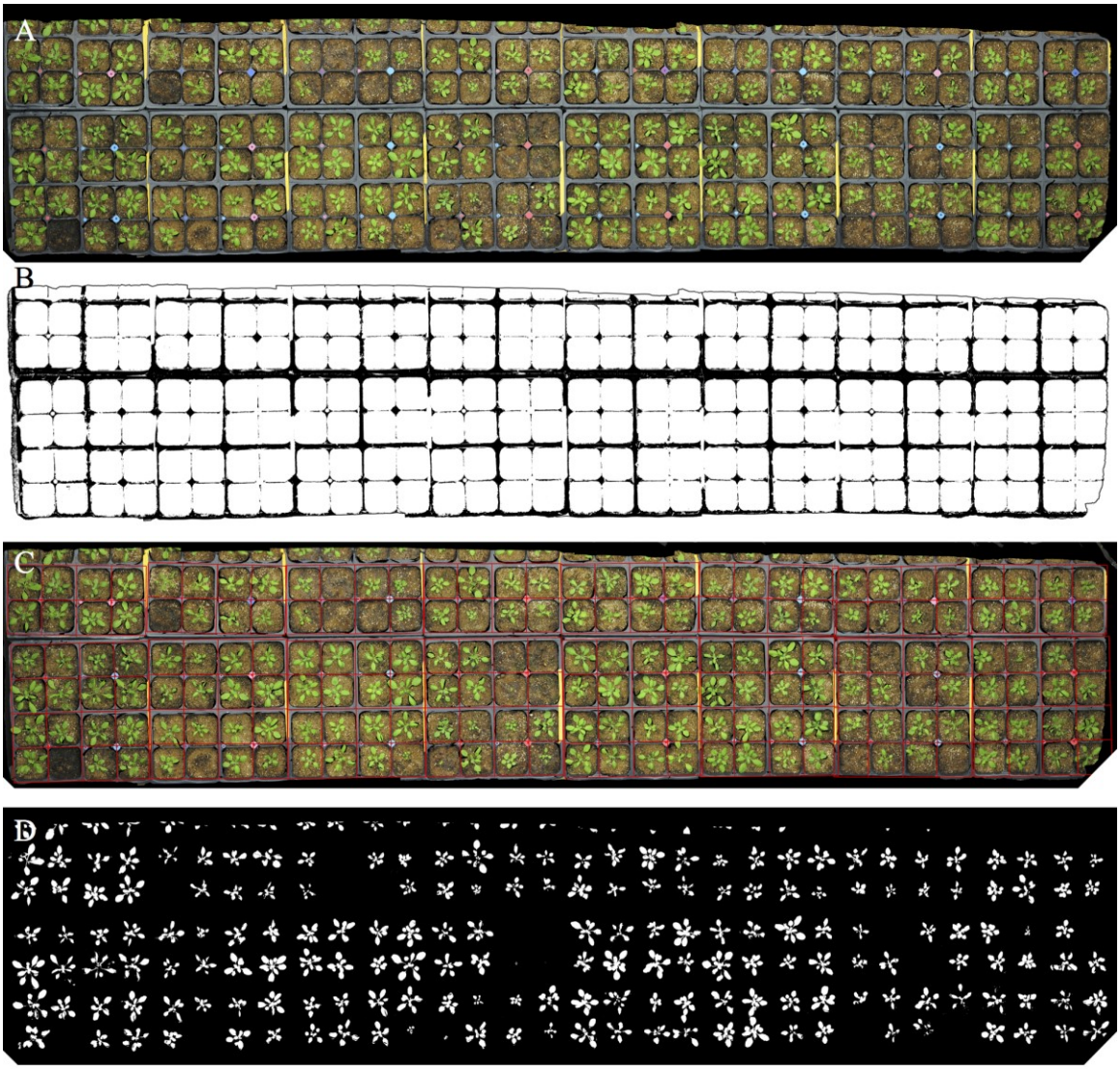

A) The mosaicked orthophoto for half-shelf; B) detected pot binary image; C) generated 4-by-4 grid overlaid on the orthophoto; D) detected plant binary image.

Figure 2.7 Field single plant extraction and genotype assignment.

The orthophoto of a plot with an automatically-generated black grid for single-plant extraction and genotype assignment.

Figure 2.8 Image optical distortion correction.

A) The image before the image optical distortion correction. The red reference line on the top shows the curvature of the edge of the color grid. B) The image after the image optical distortion correction. The edge of the color grid shows straight comparing the red reference line.

Figure 2.9 Image color correction.

A) The image before the image color correction. The green tone of the image was due to shelf illumination. B) The image after the color correction shows that the green tone was removed.

Figure 2.10 Image perspective correction.

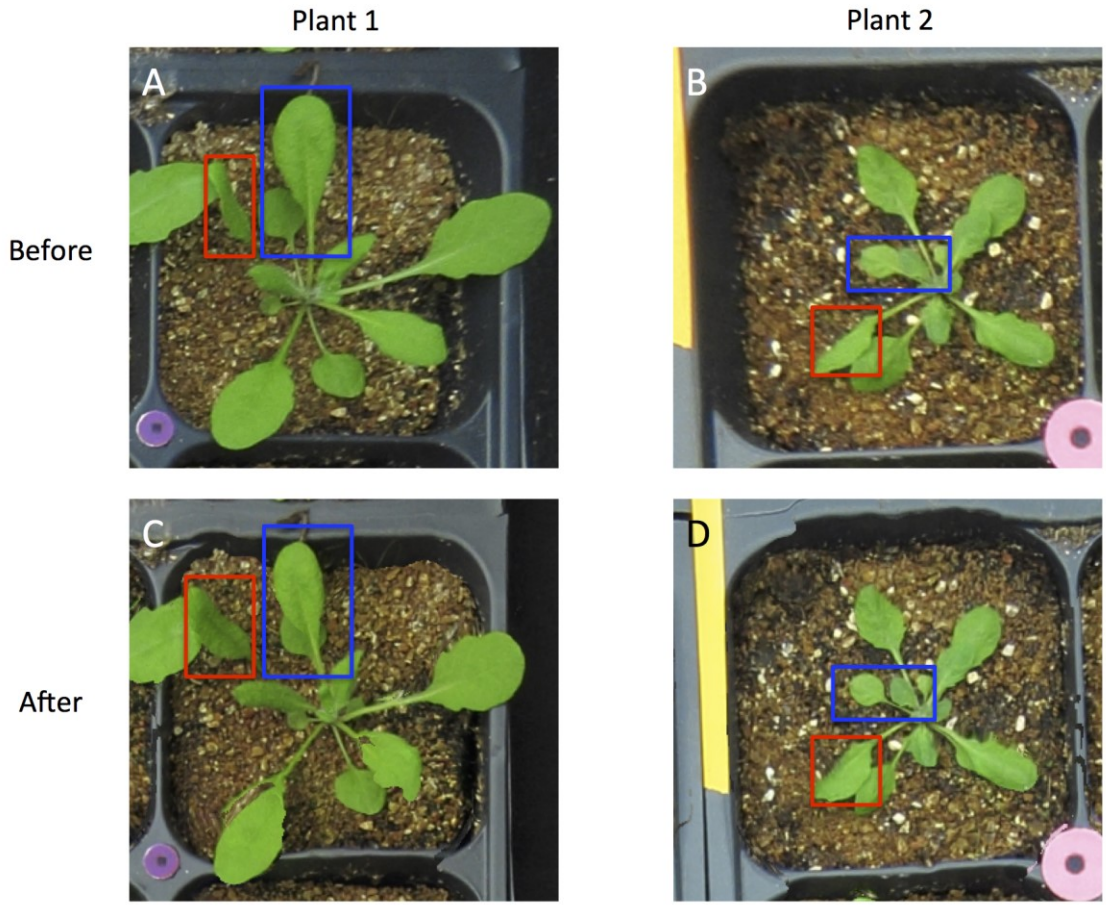

A) and B) were plant 1 and plant 2, respectively, before the perspective distortion correction, and C) and D) were the same two plants after the correction. The perspective distortion correction can: 1) show more leaf area when that leaf was not flat (as red-box–highlighted), and 2) show the corrected leaf positions (as blue-box-highlighted).

Figure 2.11 Indoor orthophoto-rendering methods comparison.

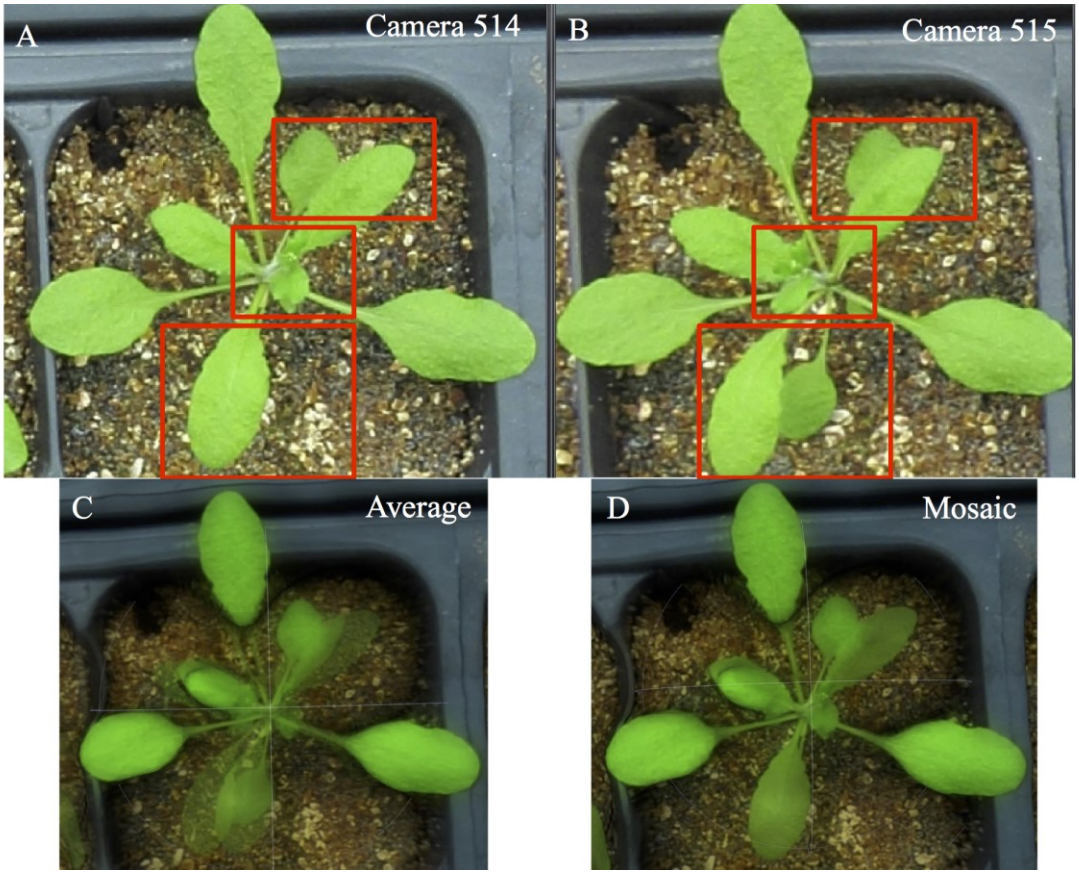

A) and B) show the same plant photographed by two adjacent cameras. The leaf positions were not consistent due to different viewing angle. When the Average rendering method was used, the "ghost-leaves" issue confused segmentation algorithm, as C) showed; Mosaic blending method could provide better image for segmentation, as D) showed.

Figure 2.12 Field orthophoto-rendering methods comparison.

A) is the ground-level plot orthophoto using Mosaic blending method; B) is the orthophoto for the same plot using Average blending method. Notice that the side-bar shadows were minimized by Average blending method.

Figure 2.13 First iteration of leaf tip detection.

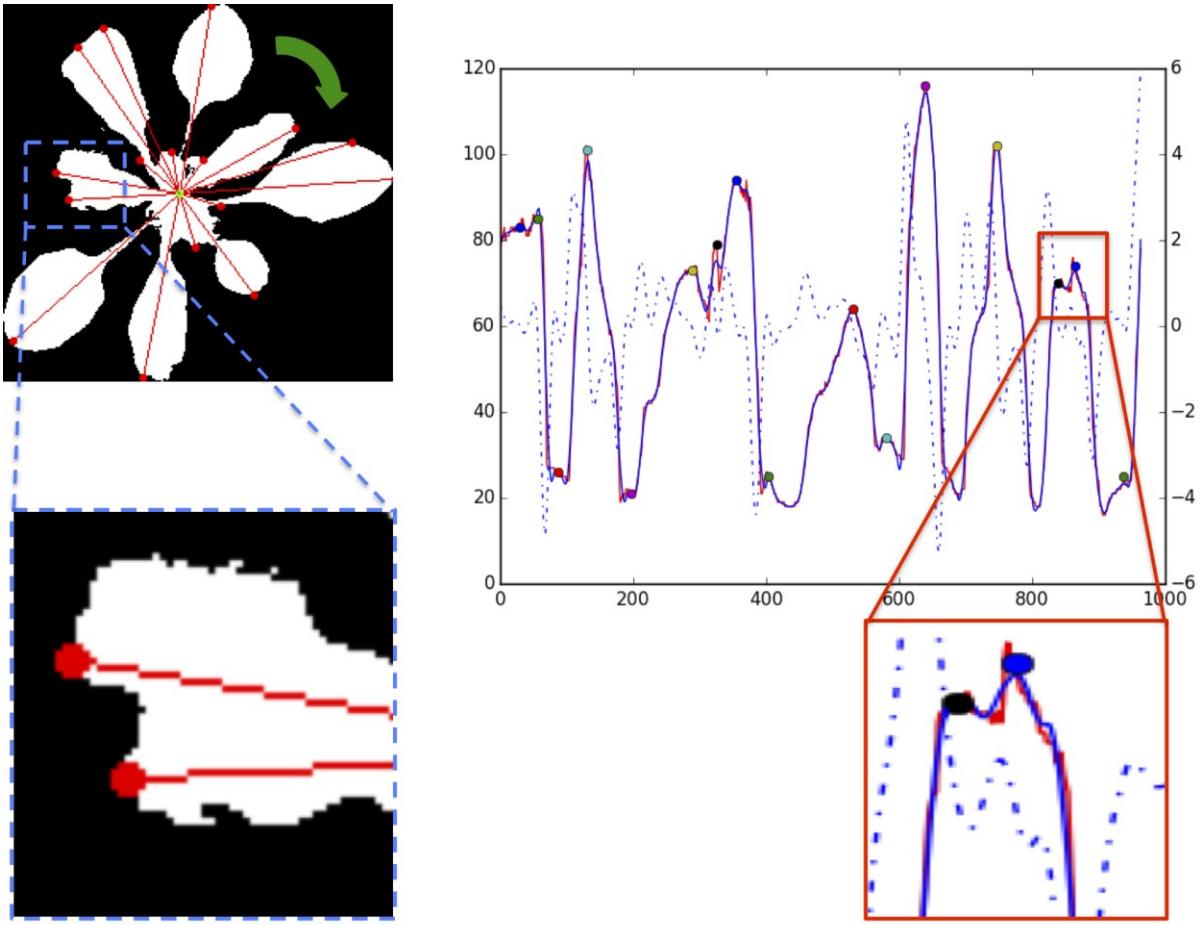

The first iteration of the Chebyshev Polynomial fitting for detecting the peaks of the rosette-outline curve, then the corresponding leaf tips on the single-rosette binary image can be found. In the plot, the red curve is the original outline curve, the blue curve is the Chebyshev Polynomial fitting curve, and the blue-dashed curve is the first derivative of the fitted curve. A damaged leave (as pictured zoomed-in) can show false tips due to the roughness or the damage of leaf edges. The corresponding plant outline curve and peaks are also highlighted. The green-curved arrow shows the direction of the radial scan.

Figure 2.14 Second iteration of leaf tip detection.

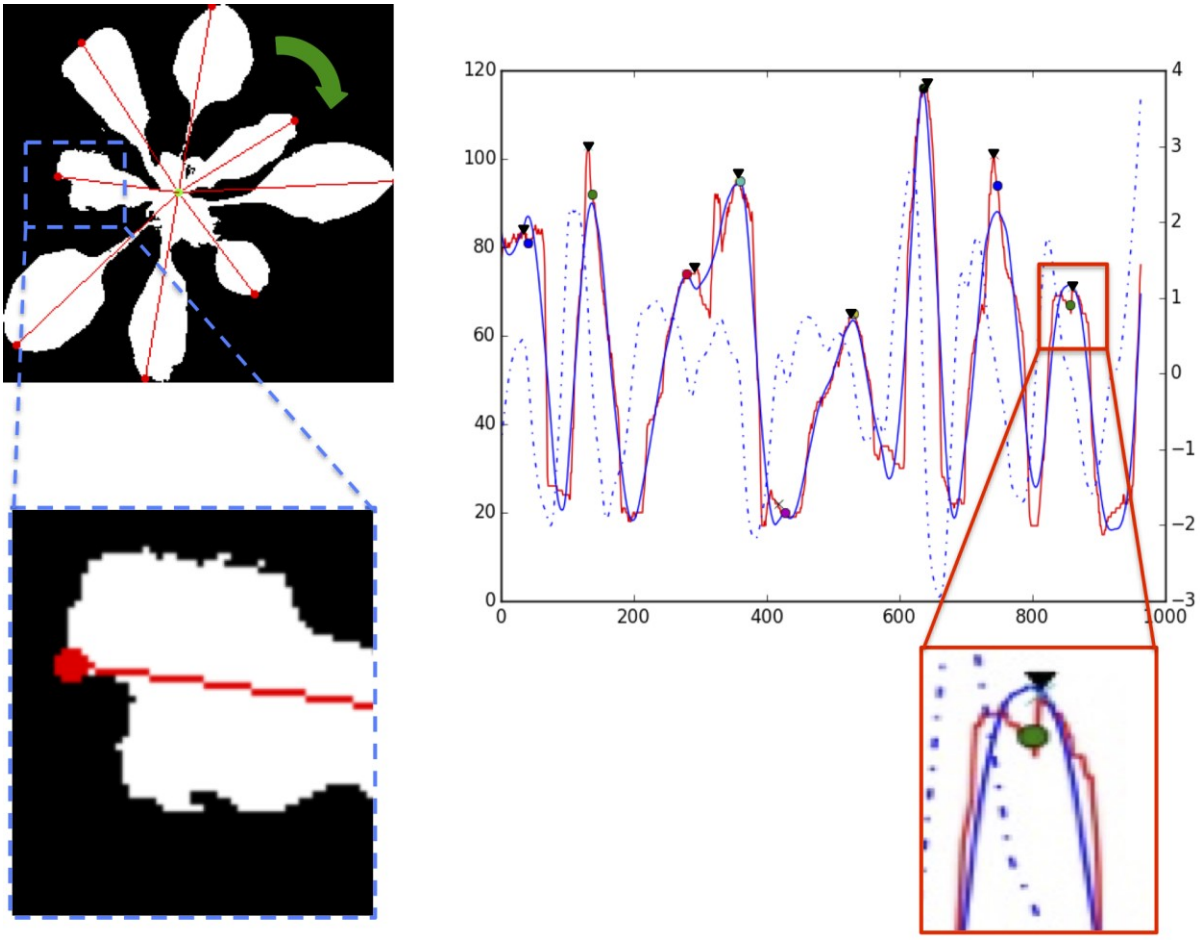

The second iteration for running the optimization algorithms. A smoother curve was fitted to the original outline curve and then a moving window was centered at each peak to locate the highest peak (black triangle markers on the curve) in the window. The zoomed-in view shows that a better leaf tip is detected. The zoomed-in view of the curve shows that the corresponding peak of the original outline curve (red curve) is detected at the black triangle marker. The true leaf tips could be relocated on the binary image.

Figure 2.15 Relationship of rosette area and total leaf expansion for indoor environment

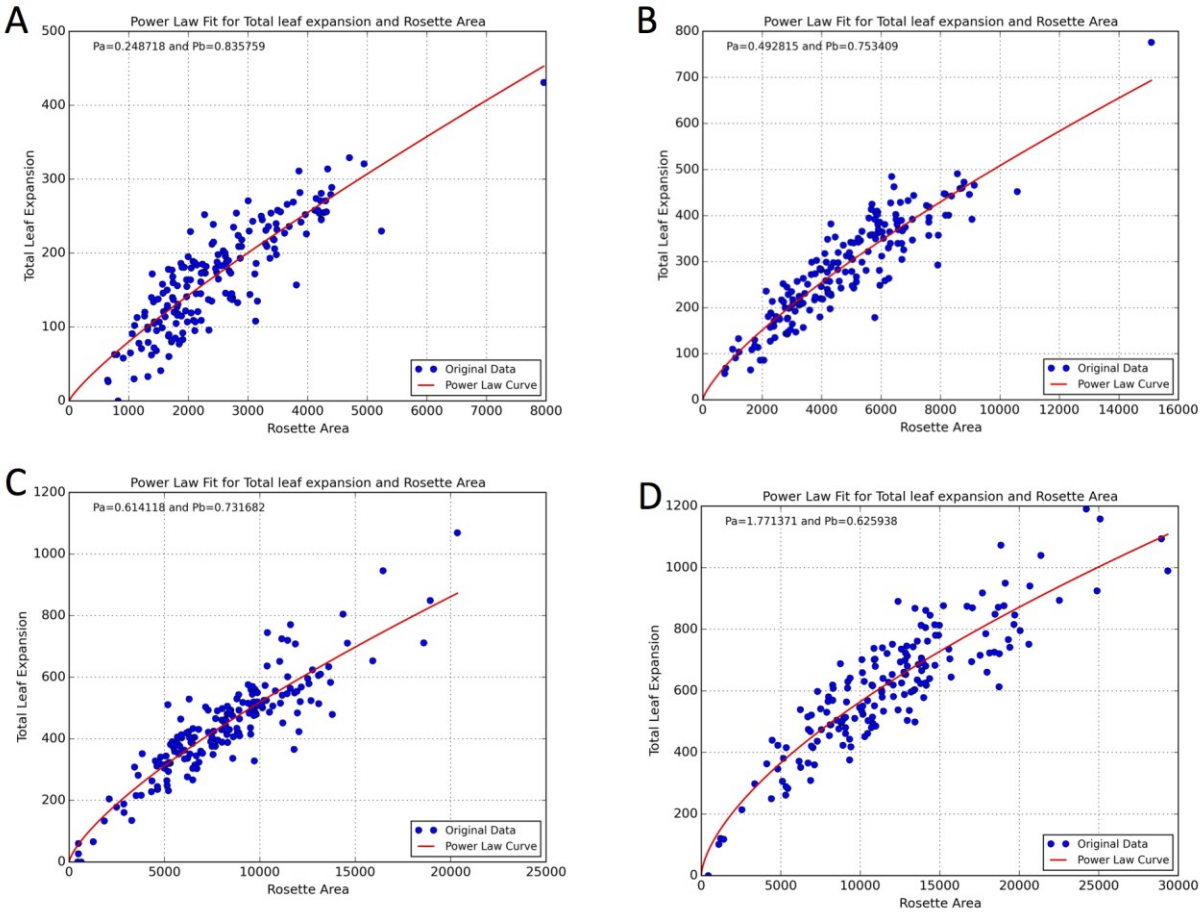

The relationship between rosette area and total leaf expansion was fitted with a power law function. The exponents of the power law function decrease from Day 1 (the eighth day after plant emergence) to Day 4 (the fourteenth day after plant emergence). At the early developmental stage, the exponent is close to 1 (as linear relationship), and at the late developmental stage, the exponent is close to 0.5, matching a previous study.

Figure 2.16 Parameter estimations for indoor environment.

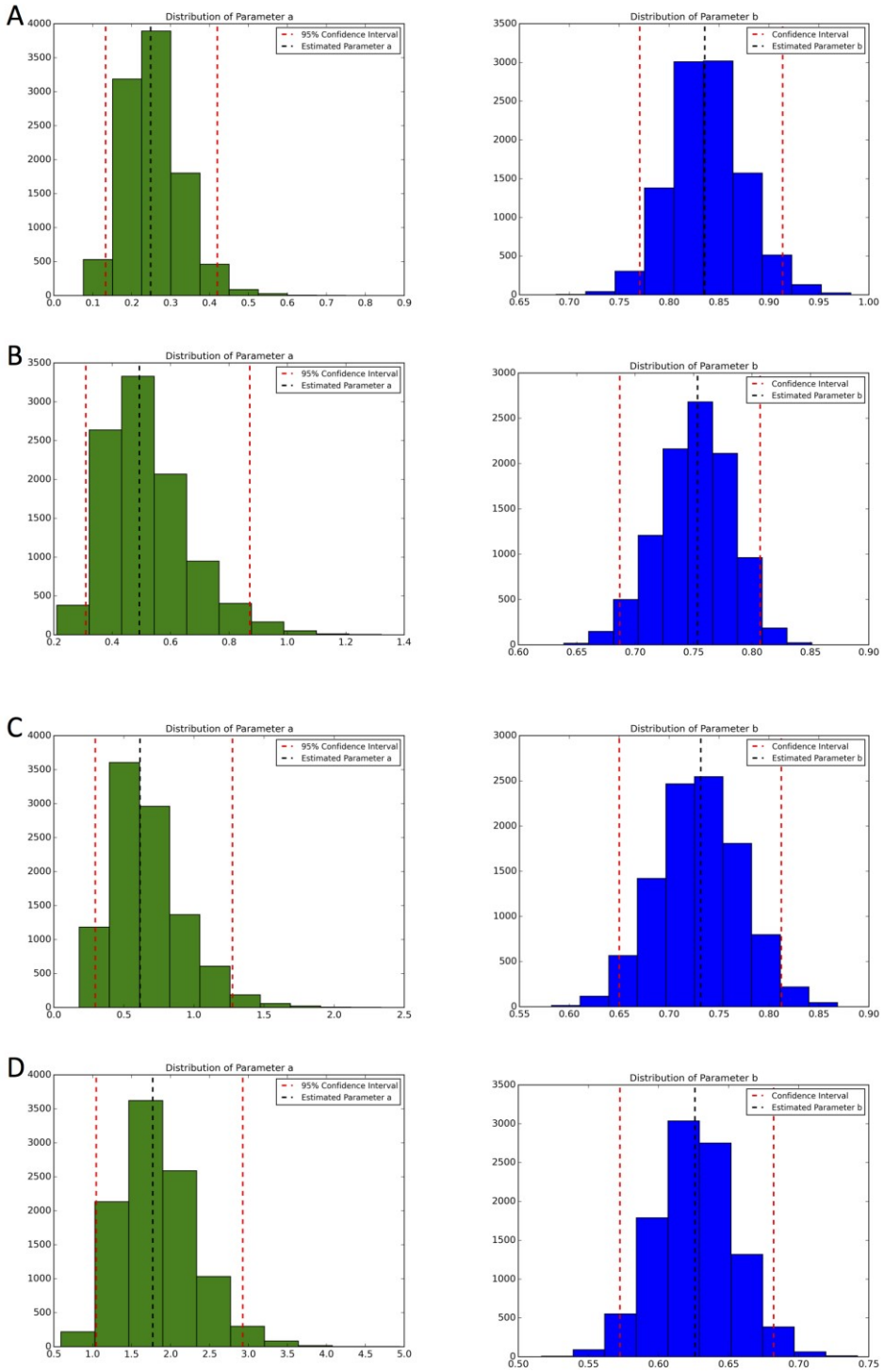

The distribution histograms of the parameters *a* and *b* of four different time points. Figure A) to D) stands for Day 1 to Day 4, respectively. The green histograms are the distributions for parameter *a* and the blue histograms are for parameter *b*. Red-dashed lines stand for 95% confidence intervals and black-dashed lines are estimated parameters.

Figure 2.17 Relationship of rosette area and total leaf expansion for field environment.

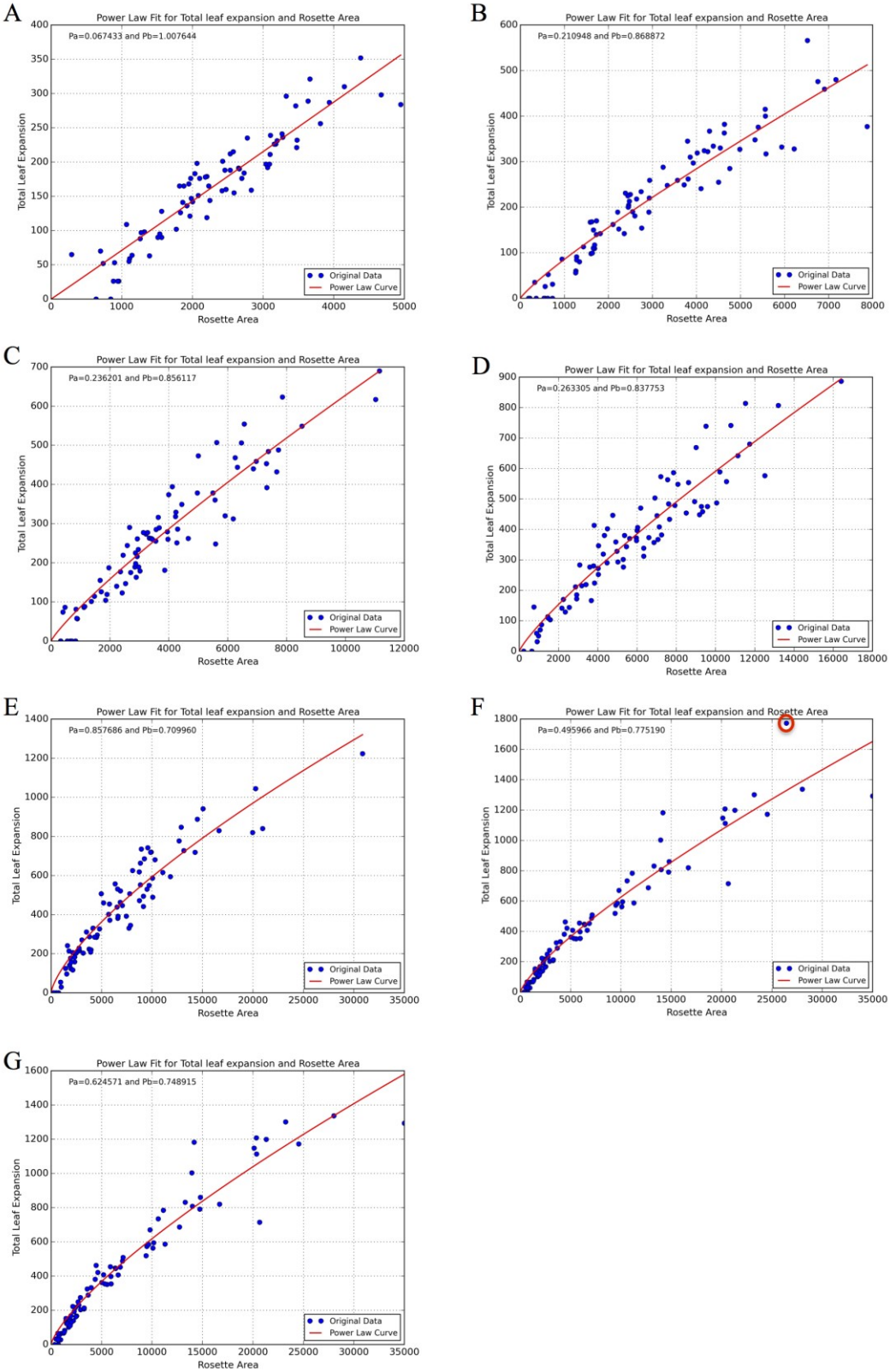

The highlighted data point in F) is an outlier. G) is the same as last day after outlier removed.

Figure 2.18 Parameter estimations for field environment.

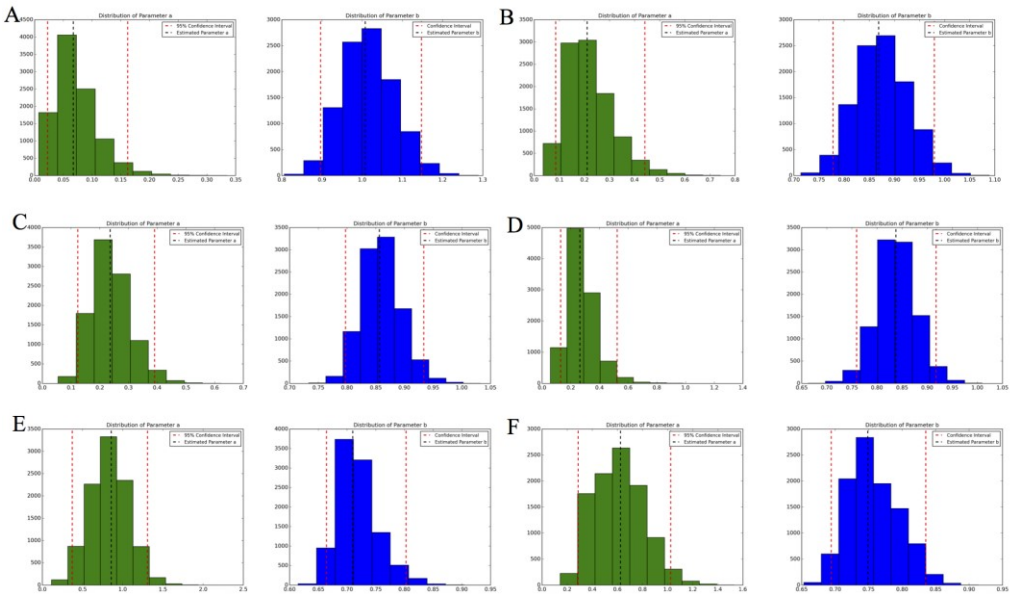

The analyses of the parameter distributions and the bootstrap 95% confidence intervals.

Figure 2.19 Original image and analyzed image of the outlier.

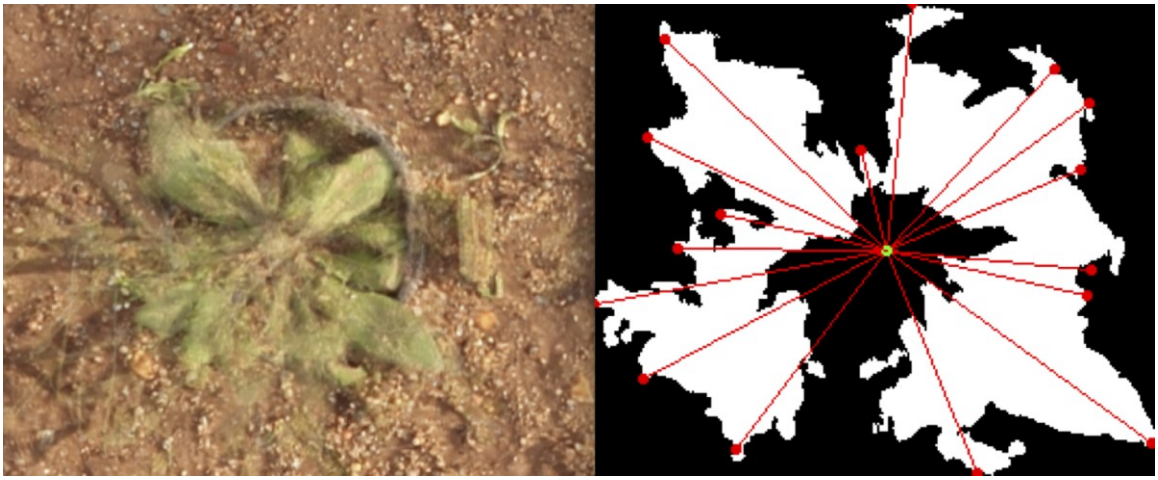

Highlights outlier from Figure 2.17F. This plant started bolting on Day 6, which lead to a confusing orthophoto. The segmented binary image missed the plant's central section and false leaf tips caused by bolting were detected, which caused reduced rosette area but increased total leaf expansion.

Table 2.1 Throughput capability of chamber phenotyping processing pipeline.

Hourly throughput (plants h^{-1} $node^{-1}$)	Average processing time per plant (s)	Average processing time for daily single-rosette images (cluster h)	Plant density (plants m^{-1})
329	10.94	11.2	225

Table 2.2 The statistics of the parameter estimation for indoor environment.

Date	Parameter	Estimation	Mean	Median	Mode	Confidence Intervals
Day 1	*a*	0.249	0.254	0.247	0.240	0.132 - 0.420
	b	0.836	0.838	0.837	0.840	0.770 - 0.913
Day 2	*a*	0.493	0.520	0.497	0.499	0.311 - 0.857
	b	0.753	0.751	0.752	0.751	0.689 - 0.807
Day 3	*a*	0.614	0.669	0.620	0.513	0.301 - 1.291
	b	0.732	0.730	0.731	0.725	0.649 - 0.811
Day 4	*a*	1.771	1.833	1.785	1.582	1.035 - 2.908
	b	0.626	0.626	0.625	0.621	0.573 - 0.683

Table 2.3 The statistics of the parameter estimation for field environment.

Date	Parameter	Estimation	Mean	Median	Mode	Confidence Intervals
Day 1	*a*	0.067	0.072	0.065	0.066	0.023 - 0.162
	b	1.008	1.015	1.012	1.013	0.896 - 1.147
Day 2	*a*	0.211	0.219	0.203	0.215	0.086 - 0.441
	b	0.869	0.875	0.873	0.871	0.778 - 0.980
Day 3	*a*	0.236	0.239	0.233	0.235	0.123 - 0.391
	b	0.856	0.859	0.858	0.857	0.797 - 0.934
Day 4	*a*	0.263	0.279	0.264	0.269	0.130 - 0.523
	b	0.838	0.838	0.837	0.837	0.759 - 0.918
Day 5	*a*	0.858	0.831	0.829	0.849	0.372 - 1.307
	b	0.710	0.719	0.713	0.715	0.664 - 0.803
Day 6	*a*	0.625	0.611	0.603	0.615	0.287 - 1.025
	b	0.749	0.757	0.752	0.754	0.694 - 0.835

Chapter 3 - 2D and 3D Pipeline results analyses

Introduction

High-throughput plant phenotyping approaches have gained tremendous interest in recent years. Such non-invasive approaches are essential to improve the efficiency and accuracy of plant phenotyping, which is critical to understanding how plant phenotypes are linked to genotypes and the surrounding environment (Furbank and Tester 2011; Fiorani and Schurr 2013; Dhondt et al. 2013; Kjaer and Ottosen 2015). Various sensors, such as 3D laser scanning sensors, RGB/near-infrared cameras, hyperspectral sensors, thermal imaging systems, and chlorophyll fluorescence imaging sensors, have been integrated into automated phenotyping pipelines to extract plant phenotypic traits from mapping populations (Rascher et al. 2011; Mahlein et al. 2012). Studies in large mapping populations enable detection of quantitative trait loci (QTLs), which are genomic regions that may contain genes controlling the plant feature of interest—for example, leaf area.

Leaf areas are of particular importance to many plant biology studies, including photosynthesis, stomatal conductance, and transpiration efficiency (Juenger et al. 2005). Previous studies (Candela et al. 1999; Pérez-Pérez et al. 2002; Cookson et al. 2007; Bylesjö et al. 2008; Weight et al. 2008; Backhaus et al. 2010; Ali et al. 2012; Chitwood et al. 2012; Maloof et al. 2013; Easlon et al. 2014) used imaging systems with commercial or customized software to acquire single-leaf areas and rosette area from 2D images. Invasive and destructive plant sampling methods (e.g., harvesting plant leaves) were used in these studies during imaging. Such methods do not allow any plant to be measured twice; moreover, they are highly labor-intensive, due to the number of plants needed to get sufficient data and the amount of manual work each plant requires.

Two-dimensional imaging techniques can provide useful information, such as obtaining estimates of rosette area or studying plant diurnal cycles via time-series analysis of nastic movements, which are rhythmic changes in leaf angles. Mullen et al. (2006) used image processing software to manually measure the leaf inclination angle in order to study these movements over short intervals. Hong et al. (2013), Dornbusch et al. (2014), and Greenham et al. (2015) used imaging systems to track leaf tip movements for studying leaf inclination angles and estimating circadian cycles. These and other, similar studies all reveal that nastic movements occur on 24-hour diurnal cycles. Note, however, that leaf tip tracking from a side view does not allow for simultaneous detection of leaf areas that change due to growth. On the other hand, vertical views that can see area will only be accurate once per day, when nastic movements reach an angle perpendicular to the line of sight. However, leaf area and plant canopy measurements based on 3D plant structure can provide good estimates regardless of plant nastic movements.

Modeling and analyzing plant 3D shape is a computing-expensive and time-consuming process (Paulus et al. 2013; Vos et al. 2009; El-Omari and Moselhi 2011). Typically, there are two types of sensors used for plant 3D modeling: active sensors and passive sensors. Laser sensors such as LIDAR (Light Detection And Ranging) are active sensors for sensing plant 3D shapes. They emit a laser beam and the time it takes for the reflected light to return to the sensor is used to compute a depth map or generate a 3D point cloud of the plant canopy. Point clouds are simply sets of 3D coordinates that, collectively, have the shape of the object of interest. None of the points are connected, so phenotypes of interest have to be inferred in often complex ways.

Palacín et al. (2007) used a laser sensor to scan pear trees for estimating canopy surface; Hosoi and Omasa (2009) utilized portable LIDAR imaging technology to model tomato plant canopy in a three-dimensional space; Keightley and Bawden (2010) and Paulus et al. (2013) used

ground-level LIDAR to estimate plant biomass. For these studies, coarse 3D measurements were sufficient, but detailed plant structures could not be studied based on these 3D models. Furthermore, the 3D measurements of these studies were not taken using an automated pipeline. Only limited numbers of plants could be analyzed during the growth period—too few for studies seeking to quantitatively relate genotypes and phenotypes within dynamic environments (Granier et al. 2006; Berger et al. 2010; Hartmann et al. 2011). Such studies can easily require mapping populations containing thousands of genetically-distinct plants.

In recent years, an increasing number of studies have used the LIDAR-based LemnaTec Scanalyzer HTS system (http://www.lemnatec.com) to obtain 3D point clouds. This system includes an automated analysis pipeline that can extract a number of phenotypic traits (Furbank and Tester 2011; Dornbusch et al 2012; Green et al. 2012; Chen et al. 2014; Dornbusch et al. 2014). However, due to the cost of such a system, it is not feasible for many smaller research laboratories and institutions.

Microsoft Kinect (https://www.microsoft.com/en-us/kinectforwindows/) is a low-cost sensor originally designed for computer gaming whose operation is based on time-of-flight measurements for a raster pattern of infrared beams. It has become a very popular choice for modeling 3D shapes in the robotic and computer vision communities. Some studies (Chéné et al. 2012; Azzari et al. 2013; Paulus et al. 2014) have evaluated it for plant phenotyping. There are, however, several issues. The throughput using Kinect is relatively low, which is not suitable for high-temporal time-series phenotyping of mapping populations. Additionally, its laser beams are not bright enough for outdoor daytime use (Azzari et al. 2013). Data can be acquired during the night but doing so is biologically problematic for the first Kinect model—its laser wavelength falls within the phytochrome absorption band. Phytochrome is a highly-sensitive plant

photoreceptor with many roles in the control of plant processes. The just-released second Kinect model uses a longer wavelength that does not have this problem.

The second approach is to use passive sensors—in particular, digital cameras—along with photogrammetric techniques to capture three-dimensional models of plants. The major advantage of these techniques is that because they are based on images, they can produce much more detailed information about the surface features being imaged than laser-based scanning can. This information is contained in a *texture image* that is painted onto the 3D model when it is displayed. Furthermore, because a texture image *is* an image, it can be subjected to common image processing techniques to extract useful information. Finally, digital cameras can be much less expensive than laser-based active sensors like LIDAR.

Previous photogrammetry work includes that of Quan et al. (2006) and Tan et al. (2007), who used the techniques to estimate camera positions and produce point clouds. They did not, however, extract any phenotypes. Quan et al. (2006) proceeded beyond point clouds *per se*, combining clustering, image segmentation, and polygon models to create 3D canopy models. These were, however, of very coarse resolution. Biskup et al. (2007) developed a stereo imaging system using two digital cameras to model soybean plants in a three-dimensional space. This, too, was a point cloud approach, but they went on to produce false color images of leaf angle. Santos and Oliveira (2012) used stereo imaging system with photogrammetric and computer vision algorithms to generate 3D models of plants, but, as above, also did not extract phenotypes. While these studies produced 3D plant canopy models, they used a small number of cameras whose positions and orientations were changed to capture different viewing angles. Although only requiring a few cameras is an advantage, the resulting low throughput does not permit highly time-resolved studies for the large number of lines in mapping populations.

In this chapter, we first demonstrate an analysis using our indoor imaging pipeline to extract time-series 2D rosette areas of a mapping population of 1050 *Arabidopsis thaliana* lines from images for studying plant nastic movement, diurnal cycles, and plant growth. Then, the pipeline was used to generate 10-day time-series of 3D models with a one-hour temporal resolution for the same plant population. In order, the pipeline color and distortion corrects raw images of potted plants on growth chamber shelves, generates 3D models of half-shelf areas, segments individual plants, pairs them with their genotypes, and then extracts time-series data of leaf growth and movement.

Materials and methods

Imaging acquisition system

The imaging acquisition process used the same indoor pipeline described in the previous chapter for studying the shade-avoidance response of a nested association mapping (NAM) population of *Arabidopsis thaliana*. In brief, 108 Canon Powershot S95 cameras were mounted facing straight down on six shelves that received two different lighting treatments. On each shelf, 18 cameras were mounted in a 2-row stationary camera frame at a 0.4-m height and photographed 24 4-by-4 pot flats hourly. A modified intervalometer script with Canon Hack Development Kit (CHDK) firmware triggered the cameras simultaneously at the beginning of each hour. In order to ensure all images had at least 50-percent overlap, the focal length of the cameras was set at 28 mm (35 mm equivalent) to maximize the field-of-view (FOV). Daytime (5:00 am to 8:00 pm) images were stored and processed for the following processes. The RAW image file format was selected for preserving all image metadata.

2D rosette analysis

Image pre-processing, orthophoto generation, single-plant extraction, and genotype assignment

The first processing steps used the same methods introduced in the previous chapter. Briefly, the Canon Digital Photo Professional (DPP) program was used for RAW image color correction, optical distortion correction, and TIFF conversion. The converted TIFF images were imported into the Agisoft Photoscan Pro (Photoscan) program (http://www.agisoft.com) to generate an orthophoto for each shelf for correcting perspective distortion, so that each pixel of orthophoto was being viewed straight down.

Each orthophoto was first segmented to a plant-only binary image using the Normalized Green–Red Difference Index (NGRDI) (Hunt et al. 2005) and the Otsu threshold method (Otsu 1975) to eliminate non-plant pixels. In a parallel step, the orthophoto was segmented to detect the pot edges to subsequently assist in isolating each plant. Segmentation was augmented by use of the probabilistic Hough Transformation (Duda and Hart 1972) to search for pot edges. The output of these steps was a set of coordinate grids delineating pot edges.

Using the color-dot system introduced in the previous chapter, the pots were tracked during the entire growth period, during which they were periodically repositioned to equilibrate environmental gradients internal to the growth chamber. Based on records made at planting, the genotype of each plant was assigned to its grid cell. Lastly, single plant binary images, each with its known genotype, were extracted from the grid cells.

2D rosette area analysis for plant nastic movement and diurnal cycle analysis

Chapter 2 reported the method we used to measure plant 2D rosette area. In this current chapter, we tracked one plant during the same 10-day growth period as in Chapter 2 and used the

Fourier Transform to study the characteristics of plant nastic movements. The hourly 2D rosette area values of the plant were calculated during this 10-day period and plotted as the black dots in Figure 10A. Because of the experimental design of the chamber study, no image data was collected during the night (9:00 pm–5:00 am). In order to extract the characteristics of the growth pattern, a linear interpolation algorithm was applied to estimate the rosette area for night hours. The Savitzky–Golay filter (Savitzky and Golay 1964) was utilized in the following step to yield a smoothed growth curve to minimize possible noise in the rosette area measurements. In order to reveal the 2D rosette area oscillation caused by the nastic movements, the Matlab detrend algorithm (http://www.mathworks.com/help/matlab/ref/detrend.html) was used to eliminate the ascending growth trend from the smoothed 10-day 2D rosette area curve. Fourier Transform was then applied to the resulting data to study the diurnal cycle.

3D rosette analysis

Camera array calibration and shelf-based 3D mesh generation

Camera calibration is the process of determining which light beam from the real world falls on which pixel of the image sensor (Bellasio et al. 2012). This entails solving for two sets of numbers. *Intrinsic parameters* specify the optical behavior of the camera itself. *Extrinsic parameters* tell where the camera is positioned in space and the direction in which it is pointing. Intrinsic parameters are often determined one camera at a time using special targets and software; however, this was not feasible due to the large number of cameras in this study. Instead, the two-row camera array of each shelf was calibrated as one imaging system using Photoscan's built-in camera calibration function.

A customized color-grid poster was printed on a shelf-size vinyl and mounted and stretched flat on each shelf surface before the experiment started. The poster was photographed

by the 18-camera array of each shelf. After pre-processing by DPP, all 18 images were imported into Photoscan to build a sparse point cloud and a dense point cloud (Figure 3.1). Photoscan first estimated camera intrinsic parameters, including the image dimension in pixels, the focal length, and the coordinates of the pixel intersected by the optical axis. Other intrinsic parameters estimated by Photoscan describe the radial and tangential lens distortion; however, early experience showed that Photoscan was not fully effective at correcting lens distortion. This is why an initial stage of lens distortion removal was first performed by DPP, as described in the previous chapter.

Photoscan next calculated the extrinsic parameters that are the X, Y, and Z coordinates of each camera's focal point and the roll, pitch, and yaw angles of the optical axis. Figure 3.1 shows the cloud of over four million points that Photoscan produced during the calibration process as well as a visual depiction of selected internal and external camera parameters. After ensuring the estimation errors of 18 camera positions were smaller than 0.5 pixels, all calibration parameters were exported to a camera calibration xml file was that was used in all subsequent analyses.

Due to a shelf design flaw described in Chapter 2, after plants were placed on the shelf, there was not enough image overlap between the two rows of cameras to build a 3D model for the entire shelf. Instead, half-shelf models were constructed, each from a set of nine images, along with the camera calibration data just described. The output was a file in Polygon File Format (PLY), which is a standard for colored 3D mesh data. Figure 3.2 shows a rendering of a half-shelf mesh model.

Single 3D plant model segmentation and plant genotype assignment

In most computer vision studies, 3D mesh segmentation is a computation-intensive and time-consuming process. For a half-shelf 3D mesh such as the one shown in Figure 3.2, there are

approximately 11 million points (vertices) connected into over 23 million faces (triangles). Locating the triangles comprising individual plants within the mesh depicting all objects in the half-shelf was nearly impossible with conventional computer vision algorithms. We developed a novel, computationally-efficient method to segment single-plant 3D models from half-shelf mesh and assign the corresponding genotype designations simultaneously. The key is the half-shelf PLY file exported from Photoscan.

There are two main sections of information contained in each PLY file. The first section contains the X, Y, Z vertex positions, unit normals (magnitude-one vectors perpendicular to the plant surface at each vertex position), and the RGB vertex colors. When the mesh is rendered, colors in between the vertices can be filled in by interpolation. Alternatively, the faces can be colored from data in a texture file which is synthesized from the original images. The latter option was used here because it provides more spatial detail.

The second section describes the triangular faces. This was done by listing the ID numbers for each of the three vertices that bound the triangle. Also listed are the 2D pixel coordinates of where each vertex is located in the orthophoto. This builds a relationship between 3D and 2D, but the linkage is one-directional. That is, from every 3D vertex one can locate a 2D pixel but from that 2D pixel one cannot easily locate its corresponding 3D vertex.

Therefore, using the methods in Chapter 2, we located binary images for each single plant, but, unlike what was done previously, they were left embedded in a background that was the same size as the orthophoto (Figure 3.3). Then, all the vertices in the mesh were scanned and the colors of their corresponding orthophoto pixels were examined. Any vertex linked to a black pixel that could not be a 3D point in the plant were not imaged in the orthophoto (Figure 3.4), and the vertices linked to the plant pixels were color-coded by the plant IDs. By using the color-

coded vertices, the vertices and faces of each plant were efficiently sorted and then extracted from the half-shelf 3D mesh. Finally, these extracted vertices and faces were exported into one PLY file in order to generate single-plant 3D models for each plant (Figure 3.5). Table 3.1 shows a section of the Python pipeline that was used for sorting and extracting vertices and faces of each plant. The beauty of this process is that, because genotype information of the single-plant binary image is assigned during its extraction, the genotype of the 3D model is automatically known.

3D area measurement for a single plant

To estimate the area of the plant, it is only necessary to sum the areas of the triangular faces of which its 3D model is composed. The area of each face was computed by: 1) converting its three vertices (A, B, and C) into two vectors, $\overrightarrow{AB}$ and $\overrightarrow{AC}$, 2) calculating the magnitude of the cross product of these two vectors, which equals the area of a parallelogram having these two vectors as sides, and 3) the face area is just half of this parallelogram's area.

Comparison between 3D and 2D area time-series

In order to compare rosette areas extracted based on 2D images and 3D models, a plant (Figure 3.6) was tracked during a 10-day growth period, and both its 2D and 3D areas were calculated every hour. Because no images were collected from 9:00 pm to 5:00 am each day, linear interpolation was used to estimate rosette area overnight. Then, the Savitzky–Golay filter (Savitzky and Golay 1964) was applied to yield a smoothed growth curve. Because the 2D and 3D systems had different units (pixel and mesh coordinates, respectively), the two areas could not be compared directly. Therefore, the values were converted to Z scores on a daily basis and plotted together for comparison. This statistical analysis was implemented in Matlab.

Results and discussion

Camera array calibration results

Figure 3.7A shows the 3D modeling results before camera calibration. Due to the linear camera array setup, the intrinsic parameters could not be estimated accurately by Photoscan because no information was available from other directions. Without correct camera intrinsic parameters, both the one-row camera array and the half-shelf 3D mesh showed curvature. The lack of information resulted because when plants were present, there was not enough vertical clearance for the fields of view of cameras in separate rows to overlap.

However, before the pots were placed on the shelf surface, the vertical space was sufficient for Photoscan to group both rows of cameras together for camera intrinsic parameter estimation. By using the camera intrinsic parameters estimated by the calibration, both the one-row camera array and the half-shelf 3D mesh are flat and the estimation errors were less than 0.5 pixels, as Figure 3.7B shows.

Plant nastic movement and diurnal cycle analysis

The black dots in Figure 3.8A are the actual time-series 2D rosette area measurements, and the red curve is the smoothed 2D rosette area curve after interpolation for no night-hour data. The oscillation caused by plant nastic movement in the red curve is visible but is distorted by the overall pattern of increasing size that will also affect the Fourier Transform results. After detrending the 2D rosette area curve (Figure 3.8B), the daily time at which this plant reaches its maximum apparent area is between 9:00 am and 10:00 am. Furthermore, the oscillation is more obvious than without curve detrending. The peak of the Fourier Transform (Figure 3.8C) is at a 24-hour frequency. This result is identical to previous studies (Hong et al. 2013; Dornbusch et al. 2014; Greenham et al. 2015) and shows that our automated pipeline can extract this data. Figure

3.8D shows the overall daily growth of the plant. The individual leaf pictures were taken at 6:00 am each day, when the leaves were most horizontal.

Time-series single-plant 3D modeling

Figure 3.9 shows the respective time-series 3D plant models for a plant during a 10-day growth period. As is clear, some petiole parts are missing. This is because some of the petioles are missing in the binary image from which the 3D image was built. However, those petiole parts contribute an insignificant amount to total plant area.

Time-series comparison between 2D area and 3D area

Figure 3.10 superimposes the day-by-day Z scores plots, directly comparing the 2D (black curve) and 3D (red curve) areas. Clearly, across the 10-day growth period, the 3D areas mainly show slow linear growth trends within each day and lack the oscillations caused by plant nastic movement in 2D areas. Also, the starting and ending measurements for both 2D and 3D curves are very close to one another within each day at times when the leaves are closest to horizontal.

Single-plant 3D modeling pipeline throughput

Table 3.2 shows the throughput capability of 3D plant area and 2D plant area. For each half-shelf, it took approximately 35 minutes for image pre-processing, orthophoto generation, 3D mesh reconstruction, binary image segmentation, and genotype assignment, thanks to GPU acceleration with OpenCL. By using optimized algorithms, it took 0.02 s on an Intel Core i7 processor to extract a single-plant 3D model from the half-shelf 3D mesh. For each plant, it took approximately 3.2 s to compute hourly 2D and 3D areas during a 10-day growth period (total: 160 plants).

Conclusion and perspectives

In this chapter, we demonstrated a novel method to: 1) reconstruct time-series shelf-based 3D meshes for NAM population of *Arabidopsis* with a stationary multi-camera array imaging system in a controlled environment, 2) analyze the time-series 2D rosette areas for studying the plant nastic movement and diurnal cycle, 3) extract each single-plant 3D model from the background 3D mesh, 4) associate it with its genotypic information, and 5) compute time-series 3D areas during a 10-day growth period. This process was integrated into our high-throughput phenotyping pipeline (described in the previous chapter) so extracting 3D plant phenotypic traits could be automated.

Comparing the plants' areas as measured from the 3D model and a corresponding 2D image during a 10-day growth period showed that both revealed increasing areas but that the 3D data was uncorrupted by plant nastic movements. This result shows that areas measured in a three-dimensional space might be more accurate and reliable when modeling and analyzing biological growth responses. Furthermore, 3D plant models can provide a unique perspective to study plant canopy structure and plant growth pattern under different environmental conditions with non-invasive and non-destructive sampling methods.

The processing time for single-plant 3D model extraction and 3D area calculation is extremely fast after applying optimized algorithms. The current limitation is the runtime for reading half-shelf 3D mesh; it is still long due to the large amount of vertices and faces of each half-shelf mesh. A further investigation on how to optimize the runtime for reading half-shelf mesh is needed.

Acknowledgement

This study was funded by the National Science Foundation Grant IOS-0923752 to Cynthia Weinig, Stephen Welch, and Julin Maloof. We are also appreciative of the helpful comments and suggestions of reviewers.

References

Ali, M. M., Al-Ani, A., Eamus, D., & Tan, D. K. (2012). A New Image-Processing-Based Technique for Measuring Leaf Dimensions. American-Eurasian Journal of Agriculture & Environmental Science, 12, 1588-1594.

Azzari, G., Goulden, M. L., & Rusu, R. B. (2013). Rapid characterization of vegetation structure with a microsoft kinect sensor. Sensors, 13(2), 2384-2398.

Backhaus, A., Kuwabara, A., Bauch, M., Monk, N., Sanguinetti, G., & Fleming, A. (2010). LEAFPROCESSOR: a new leaf phenotyping tool using contour bending energy and shape cluster analysis. New phytologist, 187(1), 251-261.

Berger, B., Parent, B., & Tester, M. (2010). High-throughput shoot imaging to study drought responses. Journal of Experimental Botany, erq201.

Bellasio, C., Olejníčková, J., Tesař, R., Šebela, D., & Nedbal, L. (2012). Computer reconstruction of plant growth and chlorophyll fluorescence emission in three spatial dimensions. Sensors, 12(1), 1052-1071.

Biskup, B., Scharr, H., Schurr, U., & Rascher, U. W. E. (2007). A stereo imaging system for measuring structural parameters of plant canopies. Plant, cell & environment, 30(10), 1299-1308.

Bylesjö, M., Segura, V., Soolanayakanahally, R.Y., Rae, A.M., Trygg, J., Gustafsson, P., Jansson, S., Street. N.R. (2008). LAMINA: a tool for rapid quantification of leaf size and shape parameters. BMC Plant Biology, 8(1), 82.

Candela, H., Martınez-Laborda, A., & Micol, J. L. (1999). Venation pattern formation in Arabidopsis thaliana vegetative leaves. Developmental biology, 205(1), 205-216.

Chen, D., Neumann, K., Friedel, S., Kilian, B., Chen, M., Altmann, T., & Klukas, C. (2014). Dissecting the phenotypic components of crop plant growth and drought responses based on high-throughput image analysis. The Plant Cell, 26(12), 4636-4655.

Chéné, Y., Rousseau, D., Lucidarme, P., Bertheloot, J., Caffier, V., Morel, P., Belin, É., Chapeau-Blondeau. F. (2012). On the use of depth camera for 3D phenotyping of entire plants. Computers and Electronics in Agriculture, 82, 122-127.

Chitwood, D.H., Headland, L.R., Filiault, D.L., Kumar, R., Jiménez-Gómez, J.M., Schrager, A.V., Park, D.S., Peng, J., Sinha, N.R., Maloof. J.N. (2012). Native environment modulates leaf size and response to simulated foliar shade across wild tomato species. PLoS One, 7(1).

Cookson, S. J., Chenu, K., & Granier, C. (2007). Day length affects the dynamics of leaf expansion and cellular development in Arabidopsis thaliana partially through floral transition timing. Annals of Botany, 99(4), 703-711.

Dhondt, S., Wuyts, N., & Inzé, D. (2013). Cell to whole-plant phenotyping: the best is yet to come. Trends in plant science, 18(8), 428-439.

Dornbusch, T., Lorrain, S., Kuznetsov, D., Fortier, A., Liechti, R., Xenarios, I., & Fankhauser, C. (2012). Measuring the diurnal pattern of leaf hyponasty and growth in Arabidopsis–a novel phenotyping approach using laser scanning. Functional Plant Biology, 39(11), 860-869.

Dornbusch, T., Michaud, O., Xenarios, I., & Fankhauser, C. (2014). Differentially phased leaf growth and movements in Arabidopsis depend on coordinated circadian and light regulation. The Plant Cell, 26(10), 3911-3921.

Duda, R. O., & Hart, P. E. (1972). Use of the Hough transformation to detect lines and curves in pictures. Communications of the ACM, 15(1), 11-15.

Easlon, H. M., & Bloom, A. J. (2014). Easy Leaf Area: Automated digital image analysis for rapid and accurate measurement of leaf area. Applications in plant sciences, 2(7).

El-Omari, S., & Moselhi, O. (2011). Integrating automated data acquisition technologies for progress reporting of construction projects. Automation in Construction, 20(6), 699-705.

Fiorani, F., & Schurr, U. (2013). Future scenarios for plant phenotyping. Annual review of plant biology, 64, 267-291.

Furbank, R. T., & Tester, M. (2011). Phenomics–technologies to relieve the phenotyping bottleneck. Trends in plant science, 16(12), 635-644.

Granier, C., Aguirrezabal, L., Chenu, K., Cookson, S. J., Dauzat, M., Hamard, P., Thioux, J., Rolland, G., Bouchier-Combaud, S., Lebaudy, A., Muller, B., Simonneau, T., Tardieu, F. (2006). PHENOPSIS, an automated platform for reproducible phenotyping of plant responses to soil water deficit in Arabidopsis thaliana permitted the identification of an accession with low sensitivity to soil water deficit. New Phytologist, 169(3), 623-635.

Green, J. M., Appel, H., Rehrig, E. M., Harnsomburana, J., Chang, J. F., Balint-Kurti, P., & Shyu, C. R. (2012). PhenoPhyte: a flexible affordable method to quantify 2D phenotypes from imagery. Plant Methods, 8(1), 1-12.

Greenham, K., Lou, P., Remsen, S. E., Farid, H., & McClung, C. R. (2015). TRiP: Tracking Rhythms in Plants, an automated leaf movement analysis program for circadian period estimation. Plant methods, 11(1), 33.

Hartmann, A., Czauderna, T., Hoffmann, R., Stein, N., & Schreiber, F. (2011). HTPheno: an image analysis pipeline for high-throughput plant phenotyping. BMC bioinformatics, 12(1), 148.

Hosoi, F., & Omasa, K. (2009). Estimating vertical plant area density profile and growth parameters of a wheat canopy at different growth stages using three-dimensional portable lidar imaging. ISPRS Journal of Photogrammetry and Remote Sensing, 64(2), 151-158.

Hong, S., Kim, S. A., Guerinot, M. L., & McClung, C. R. (2013). Reciprocal interaction of the circadian clock with the iron homeostasis network in Arabidopsis. Plant physiology, 161(2), 893-903.

Hunt Jr, E. R., Cavigelli, M., Daughtry, C. S., Mcmurtrey III, J. E., & Walthall, C. L. (2005). Evaluation of digital photography from model aircraft for remote sensing of crop biomass and nitrogen status. Precision Agriculture, 6(4), 359-378.

Juenger, T.E., Mckay, J.K., Hausmann, N., Keurentjes, J.J., Sen, S., Stowe, K.A., Dawson, T.E., Simms, E.L., Richards, J. H. (2005). Identification and characterization of QTL underlying whole-plant physiology in Arabidopsis thaliana: δ13C, stomatal conductance and transpiration efficiency. Plant, Cell & Environment, 28(6), 697-708.

Keightley, K. E., & Bawden, G. W. (2010). 3D volumetric modeling of grapevine biomass using Tripod LiDAR. Computers and Electronics in Agriculture, 74(2), 305-312.

Kjaer, K. H., & Ottosen, C. O. (2015). 3D laser triangulation for plant phenotyping in challenging environments. Sensors, 15(6), 13533-13547.

Mahlein, A. K., Oerke, E. C., Steiner, U., & Dehne, H. W. (2012). Recent advances in sensing plant diseases for precision crop protection. European Journal of Plant Pathology, 133(1), 197-209.

Maloof, J. N., Nozue, K., Mumbach, M. R., & Palmer, C. M. (2013). LeafJ: An ImageJ plugin for semi-automated leaf shape measurement. JoVE (Journal of Visualized Experiments), (71), e50028-e50028.

Mullen, J. L., Weinig, C., & Hangarter, R. P. (2006). Shade avoidance and the regulation of leaf inclination in Arabidopsis. Plant, Cell & Environment, 29(6), 1099-1106.

Otsu, N. (1975). A threshold selection method from gray-level histograms. Automatica, 11(285-296), 23-27.

Palacín, J., Pallejà, T., Tresanchez, M., Sanz, R., Llorens, J., Ribes-Dasi, M., Masip, J., Arnó, J., Escolà, A., Rosell, J.R. (2007). Real-time tree-foliage surface estimation using a ground laser scanner. Instrumentation and Measurement, IEEE Transactions on, 56(4), 1377-1383.

Paulus, S., Dupuis, J., Mahlein, A. K., & Kuhlmann, H. (2013). Surface feature based classification of plant organs from 3D laserscanned point clouds for plant phenotyping. BMC bioinformatics, 14(1), 238.

Paulus, S., Behmann, J., Mahlein, A. K., Plümer, L., & Kuhlmann, H. (2014). Low-cost 3D systems: suitable tools for plant phenotyping. Sensors, 14(2), 3001-3018.

Pérez-Pérez, J. M., Serrano-Cartagena, J., & Micol, J. L. (2002). Genetic analysis of natural variations in the architecture of Arabidopsis thaliana vegetative leaves. Genetics, 162(2), 893-915.

Quan, L., Tan, P., Zeng, G., Yuan, L., Wang, J., & Kang, S. B. (2006, July). Image-based plant modeling. In ACM Transactions on Graphics (TOG) (Vol. 25, No. 3, pp. 599-604). ACM.

Rascher, U., Blossfeld, S., Fiorani, F., Jahnke, S., Jansen, M., Kuhn, A.J., Matsubara, S., Märtin, L.L.A., Merchant, A., Metzner, R., Müller-Linow, M., Nagel, K.A., Pieruschka, R., Pinto, F., Schreiber, C.M., Temperton, V.M., Thorpe, M.R., Dusschoten, D.V., Volkenburgh, E.V., Windt, C.W., Schurr, U. (2011). Non-invasive approaches for phenotyping of enhanced performance traits in bean. Functional Plant Biology, 38(12), 968-983.

Santos, T. T., & Oliveira, A. A. (2012, August). Image-based 3D digitizing for plant architecture analysis and phenotyping. In Workshop on Industry Applications (WGARI) in SIBGRAPI 2012, 21-28.

Savitzky, A., & Golay, M. J. (1964). Smoothing and differentiation of data by simplified least squares procedures. Analytical chemistry, 36(8), 1627-1639.

Tan, P., Zeng, G., Wang, J., Kang, S. B., & Quan, L. (2007, August). Image-based tree modeling. In ACM Transactions on Graphics (TOG) 26(3), p. 87. ACM.

Vos, J., Evers, J. B., Buck-Sorlin, G. H., Andrieu, B., Chelle, M., & De Visser, P. H. (2009). Functional–structural plant modelling: a new versatile tool in crop science. Journal of experimental Botany, erp345.

Weight, C., Parnham, D., & Waites, R. (2008). TECHNICAL ADVANCE: LeafAnalyser: a computational method for rapid and large-scale analyses of leaf shape variation. The Plant Journal, 53(3), 578-586.

Figure 3.1 Camera calibration.

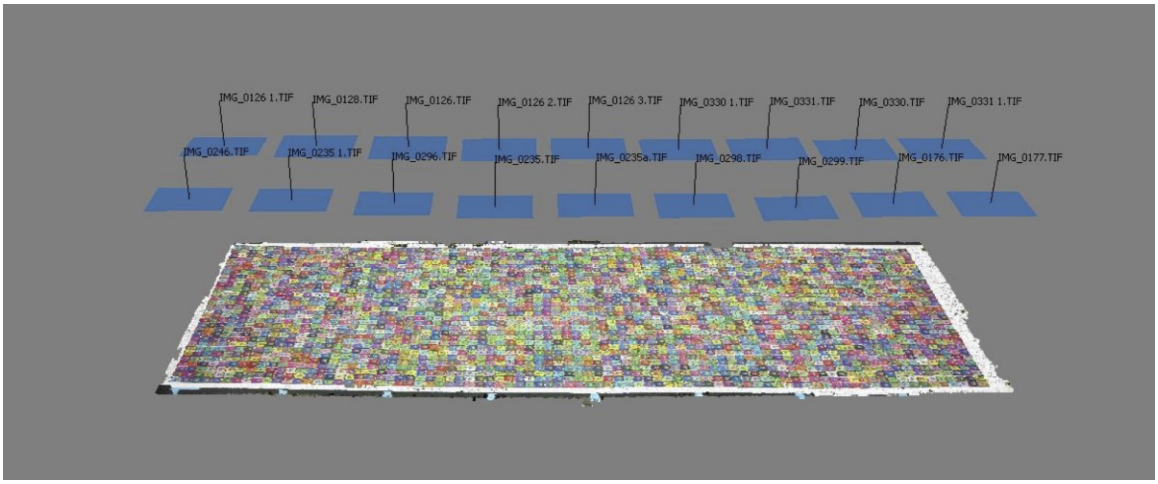

The dense point cloud in a three-dimensional space generated by Photoscan for calibrating a two-row camera system using a customized color-grid poster. The blue boxes are the estimated camera positions in a three-dimensional space; the black lines show the orientations of each camera. The camera intrinsic parameters were estimated by this process.

Figure 3.2 A half-shelf 3D mesh generated by Photoscan.

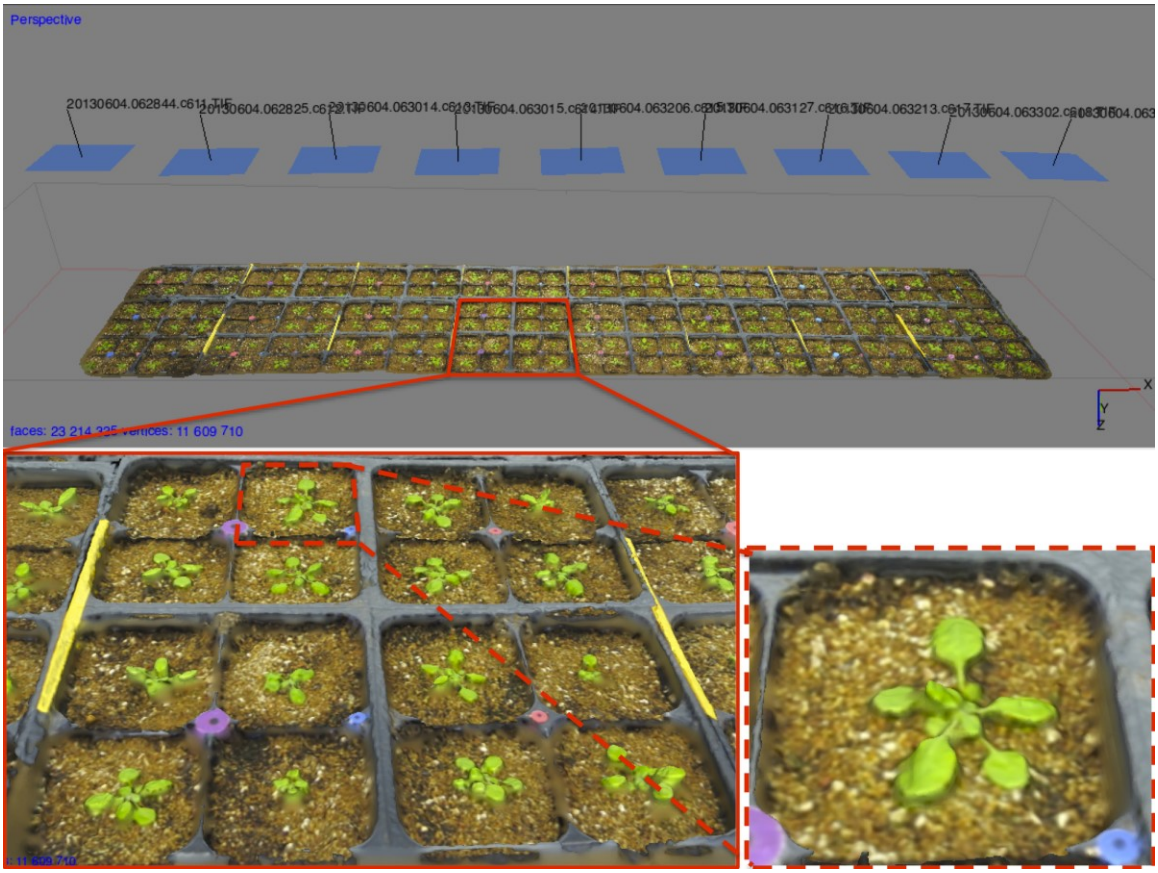

The top center is the 3D mesh generated by one-row camera array; the lower-left is a close-up view for one 4-by-4 flat; the lower right is a close-up view for one plant.

Figure 3.3 Single-plant binary image for extracting a single-plant 3D model.

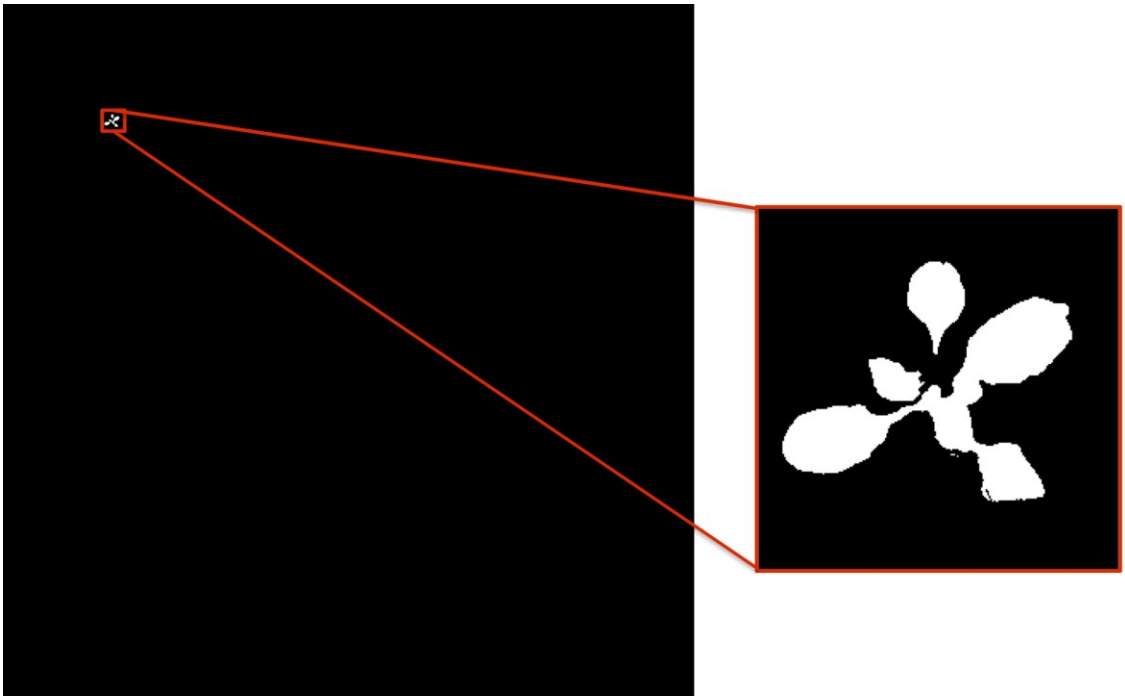

Left: A single-plant binary image with the original orthophoto's dimension. The black area in the left image is used to eliminate the non-related mesh. Right: the close-up view of this plant.

Figure 3.4 A single-plant vertex map.

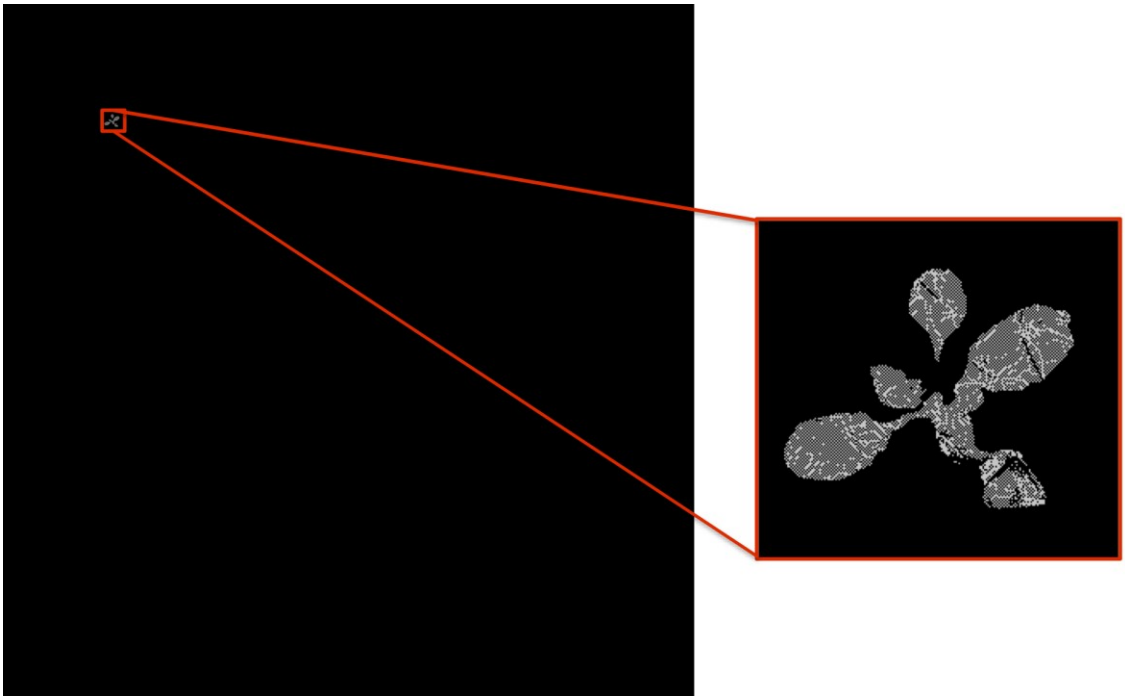

Left: A single-plant vertex map for representing the saved vertices of the 3D mesh. The grey pixels stand for the saved corresponding vertices from the half-shelf 3D mesh. Black area means that the corresponding area on the mesh was eliminated. Right: the close-up view of this vertex map.

Figure 3.5 A single-plant 3D model.

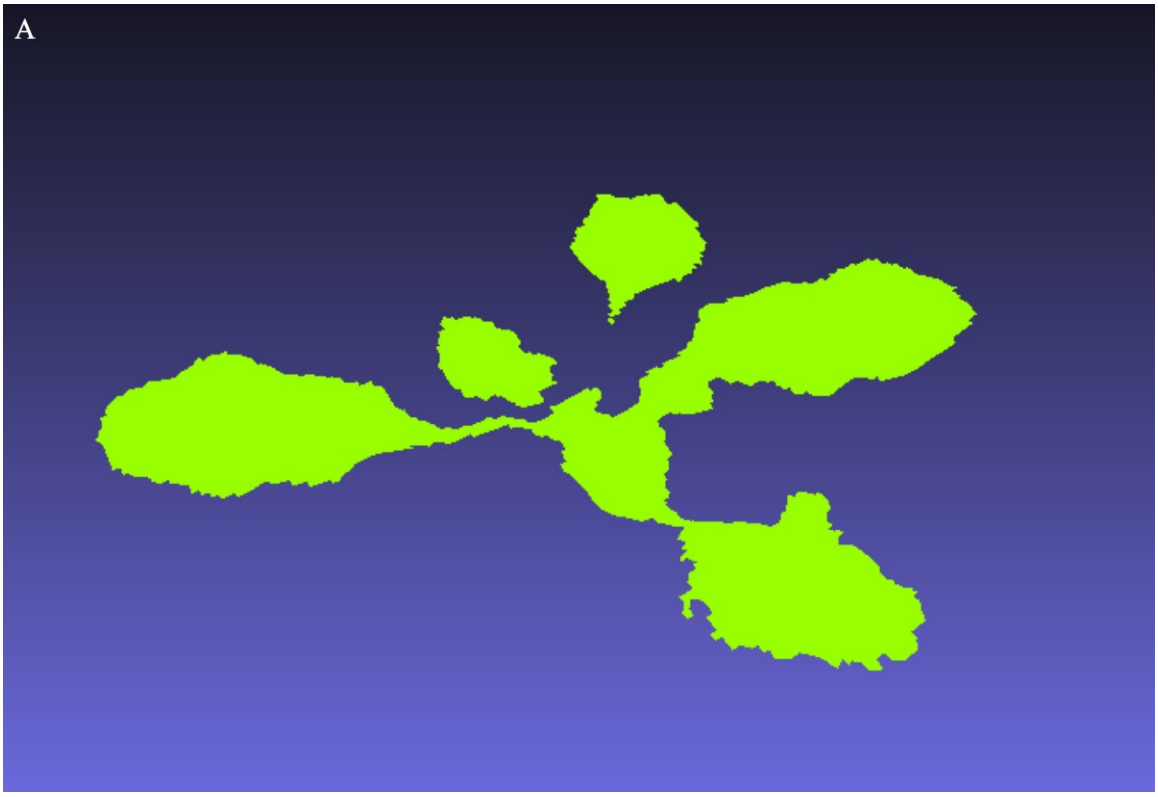

The extracted single-plant 3D model viewed from two different angles.

Figure 3.6 Plant orthophoto vs. 3D model.

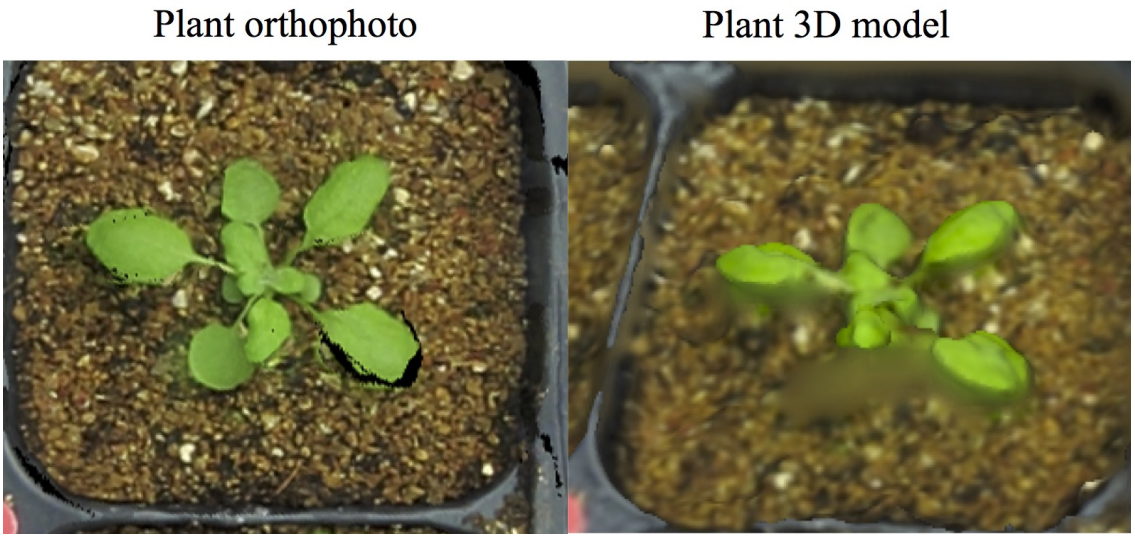

One sample plant was analyzed in this article. The left image is the orthophoto of this plant, and the right image is its 3D model before single-plant 3D model extraction.

Figure 3.7 Half-shelf 3D mesh before and after camera calibration.

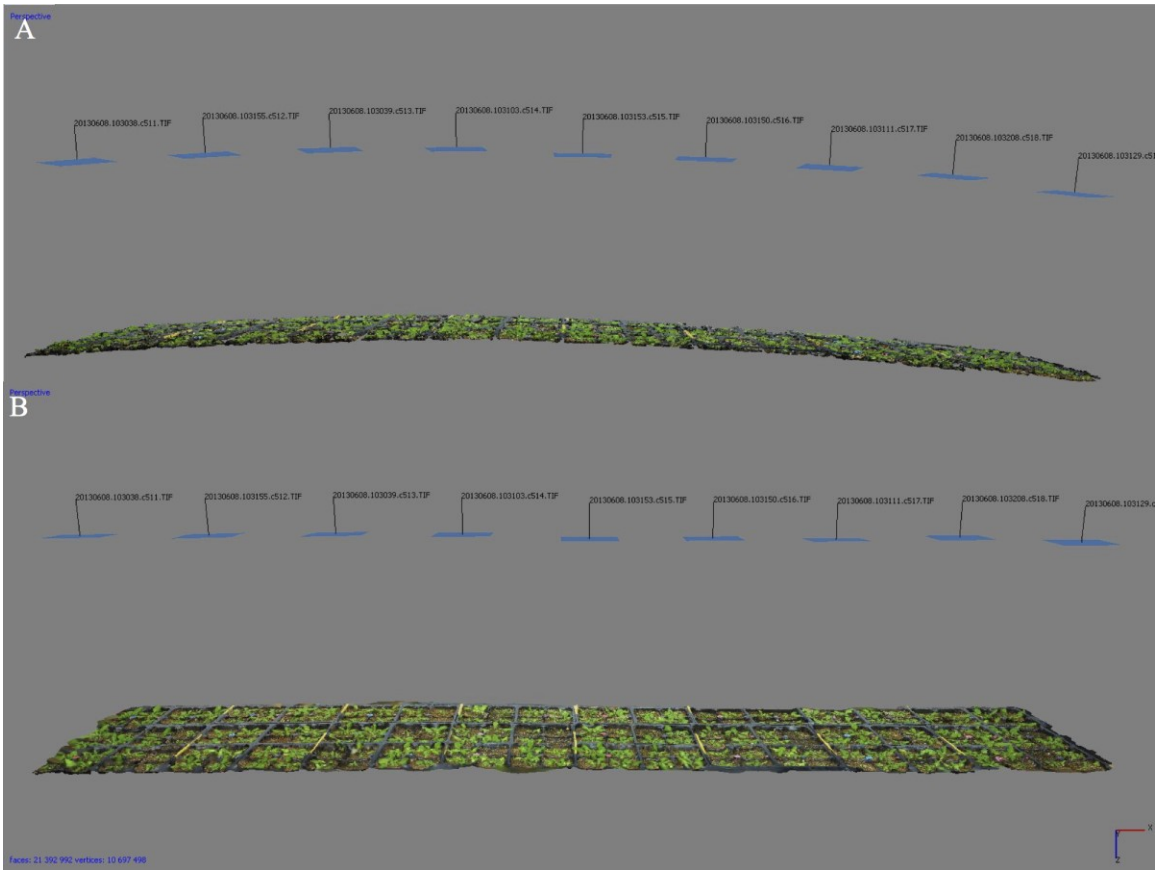

A) The half-shelf 3D mesh showed curvature before camera calibration. No plant area could be estimated at this point. B) The same model with accurate camera intrinsic parameters; the 3D mesh was flat.

Figure 3.8 Plant nastic movement and diurnal cycle analysis.

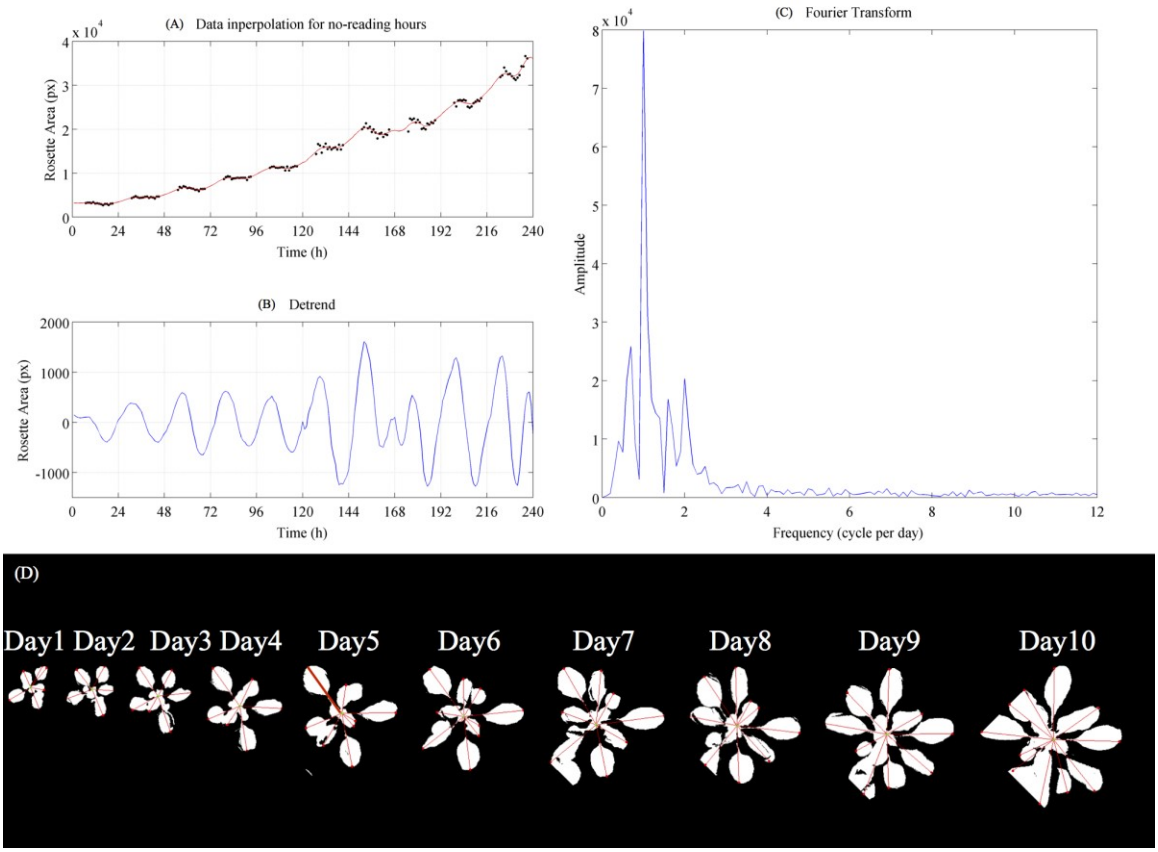

A) The graph is the 16-hour rosette area measurements (black dots) and smoothed growth curve (red curve); B) the detrended plant growth curve to show the plant nastic movement; C) the Fourier Transform to the diurnal movement is a daily cycle; D) time-series single-rosette binary images for this plant.

Figure 3.9 Time-series 3D models.

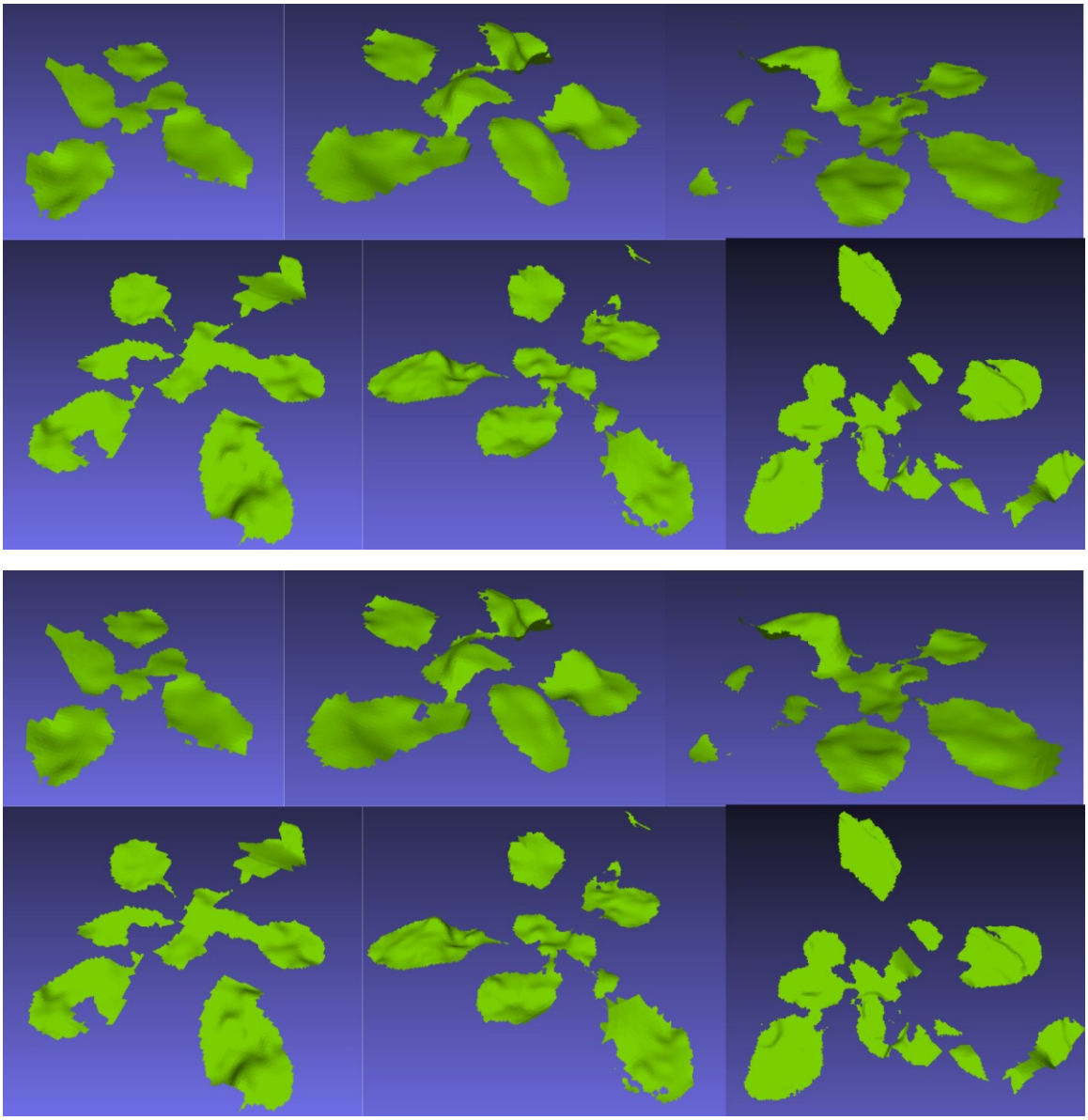

Time-series single-plant models during a 10-day growth period.

Figure 3.10 Z score comparison between 3D area and 2D area.

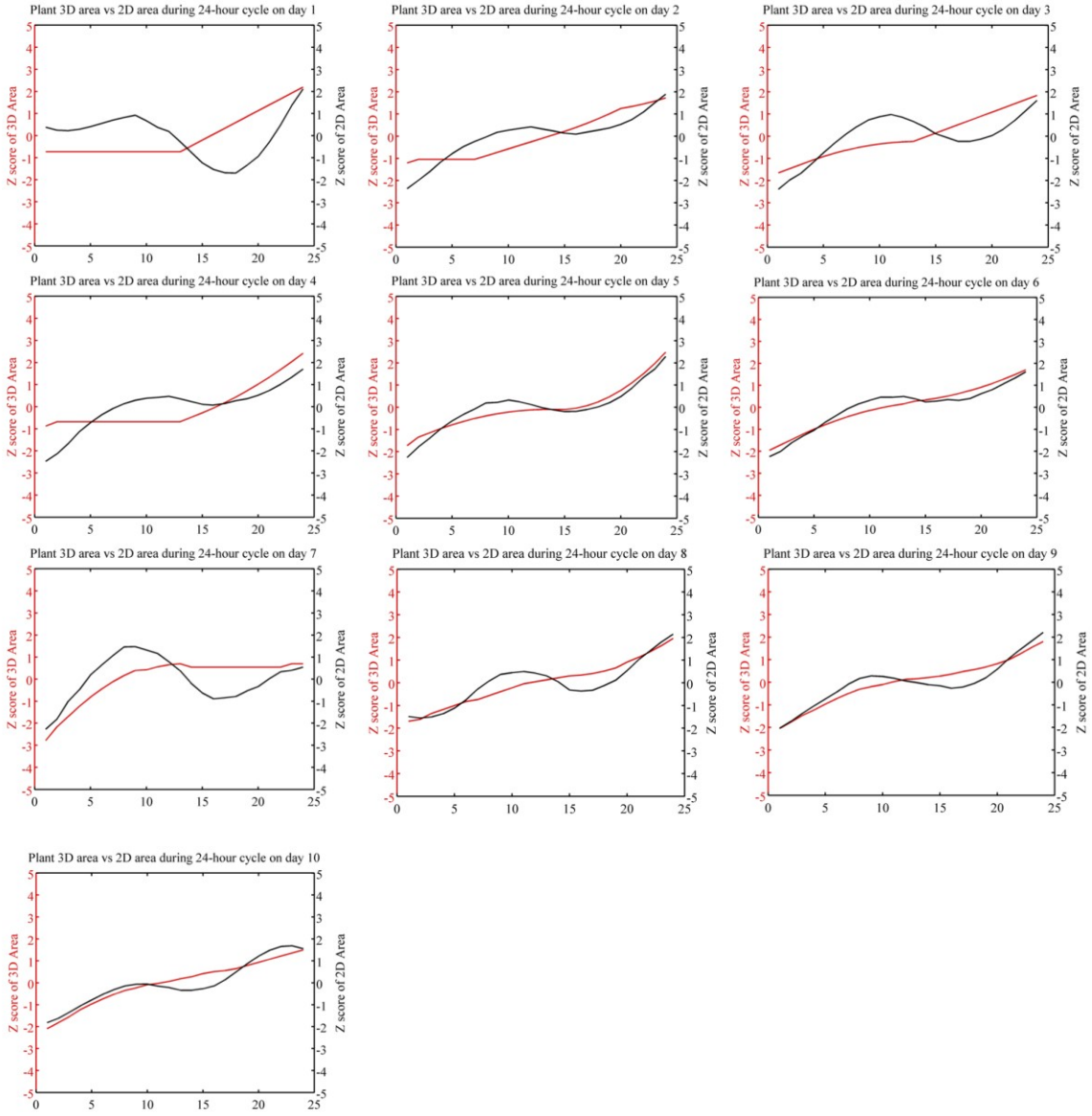

Daily Z scores comparisons between 3D areas (red curve) and 2D areas (black curve) during a 10-day growth period.

Table 3.1 Sample Python code for sorting and extracting plant vertices and faces.

```
Plant_verticesList = np.sort(existingPlant+[0])

FCodes = np.min(plant_idx[M.PixelX_vertex[M.Faces],M.PixelY_vertex[M.Faces]],axis=1)

FIndex = np.argsort(FCodes)
FBreaks = np.searchsorted(FCodes[FIndex], Plant_verticesList,side='right')

# extracting the vertices and faces for each plant
Areas_3D = np.zeros(len(coord))
for i in range(0,len(existingPlant)):
        start_SinglePlant = timeit.default_timer()
        plant = Mesh()
        plant_face = M.Faces[FIndex[FBreaks[i]:FBreaks[i+1]]]
        plant_faceReshape = np.reshape(plant_face, -1)
        plant_vertex = np.unique(plant_face)
        plant_vertexIDX = range(0, len(plant_vertex))
        # build a dictionary for old vertex and new vertex
        Idx_dict = dict(zip(plant_vertex, plant_vertexIDX))
        plant_FaceNewIDX = [Idx_dict[j] for j in plant_faceReshape]
        # reshape back the Faces for new plant mesh
        plant_NewFaces = np.reshape(plant_FaceNewIDX, (-1,3))
        plant.Faces = plant_NewFaces
        plant.XYZ = M.XYZ[plant_vertex]
        plant.NRM = M.NRM[plant_vertex]
        plant.RGB = M.RGB[plant_vertex]

if list(plant.Faces)==[]: # if the plant does not exist
        Areas_3D[existingPlant[i]-1]=0
else:
        plant.FaceAreas()
        Areas_3D[existingPlant[i]-1] = sum(plant.Areas)
        plant.WriteSelectedPoints(path+filename+'_3Dplant_'+str(FCodes[FIndex[FBreaks[i]]]),
        Data="ASCII")
```

Table 3.2 Throughput capability of single-plant 3D and 2D area calculation.

Average processing time per half-shelf (s)	Average processing time per plant (s)	Average runtime for hourly single-plant area during 10-day period (cluster s)
3.84	0.02	3.2

Chapter 4 - Conclusion

The bottleneck of conventional phenotyping methods has limited the ability to understand the interaction between a plant's genotype and its surrounding environment. In particular, invasive and destructive sampling methods, along with the traditional measuring techniques widely used in conventional phenotyping, are labor-intensive, time-consuming, costly, and can easily lack consistency across workers. These traits impede large-scale genetic studies within plant biology and crop production.

The high-throughput phenotyping pipeline presented in this study shows significant potential for large-scale noninvasive plant measurement using photogrammetry and 3D modeling techniques in the model species, *Arabidopsis thaliana*. This not only supports improved understanding of plant growth and development in a time-series manner but also can help determine the performance of specific genotypes by analyzing whole-plant phenotypic traits in different environments. The main features of the pipeline include: noninvasive 2D imaging and 3D reconstruction, elements of instrument independency with cross-platform capability, and customizable pipeline design.

Noninvasive 2D imaging and 3D reconstruction automates image data collection, transfer, storing, management, processing, analysis, and the extraction of phenotypes. This automated pipeline makes it possible to phenotype a large mapping population of *Arabidopsis* at one-hour intervals—something that could not be done by purely manual methods. The 2D image analyses in the pipeline utilizes remote sensing image processing methods that allow us to quickly measure the apparent lengths of all leaves, as well as analyze plant nastic movements and diurnal cycles. 3D plant reconstruction and segmentation by the pipeline allows us to

separate out the effects of nastic movements and, therefore, to accurately and efficiently measure genotypic rosette area growth increases for different genotypes.

Elements of instrument independency within this pipeline eliminate specific imaging system requirements by using high-level scripting language for pipeline automation. Unlike high-throughput phenotyping methods presented in other studies, this feature improves our pipeline flexibility regardless of differences in manufacturer-provided software. With minimal alterations (mainly rewriting short scripts), one imaging system and its corresponding vendor-supplied software could be easily replaced by another without changing other portions of the pipeline.

Cross-platform capability is the main difference and advantage of this system compared to other high-throughput phenotyping pipelines. Although this pipeline was developed based on *Arabidopsis* for studying shade-avoidance responses in a controlled indoor environment, it was shown to be sufficiently generic that it could be transferred into a field environment with minimal or no alteration. For future work, the pipeline may be scaled up using other ground-level or even aerial-level imaging platforms in the field environment for phenotyping different plants and crops.

Customizable pipeline design allows us to integrate advanced analysis methods into the pipeline in the future. Quantitative statistics are routinely used to create models based on phenotype and genotype data, and environmental inputs are becoming more important in these and other types of models. The customizable characteristics of this pipeline support integration of various modeling methods into the pipeline in order to reduce the complexity of data analysis of large-scale genetic studies. For example, one might readily envision integrating a genetic

mapping program into the pipeline. The pipeline in this study showed its versatility in analyzing different plant phenotypic traits with different modeling methods.

Finally, the future phenotypic landscape is becoming increasingly more complex. Therefore, successful high-throughput phenotyping pipelines need to possess the competence to integrate interdisciplinary tools and technologies comprising agronomy, plant physiology, plant genetics, breeding, computer science, remote sensing, engineering, and mathematical modeling. Furthermore, phenotyping pipelines must also be suitable for working in different environments and on different platforms. The high-throughput phenotyping pipeline presented in this study fulfills these two requirements. Such a pipeline will show its versatility by helping to find solutions to crop production and plant biology problems.